

# The JCMT Legacy Survey of the Gould Belt: a molecular line study of the Ophiuchus molecular cloud

Glenn J. White<sup>1,2</sup>, Emily Drabek-Maunder<sup>3,11</sup>, Erik Rosolowsky<sup>4</sup>, Derek Ward-Thompson<sup>5</sup>, C.J. Davis<sup>8</sup>, Jon Gregson<sup>2</sup>, Jenny Hatchell<sup>3</sup>, Mireya Etxaluze<sup>2</sup>, Sarah Stickler<sup>4</sup>, Jane Buckle<sup>7</sup>, Doug Johnstone<sup>6,9,15</sup>, Rachel Friesen<sup>14</sup>, Sarah Sadavoy<sup>9</sup>, Kieran. V. Natt<sup>1</sup>, Malcolm Currie<sup>9</sup>, J. S. Richer<sup>7</sup>, Kate Pattle<sup>5</sup> Marco Spaans<sup>10</sup>, James Di Francesco<sup>6,12</sup>, M.R. Hogerheijde<sup>13</sup>

<sup>1</sup> *RALSpace, The Rutherford Appleton Laboratory, Chilton, Didcot, Oxfordshire, OX11 0QX, England*

<sup>2</sup> *Department of Physics and Astronomy, The Open University, Walton Hall, Milton Keynes, MK7 6AA, England*

<sup>3</sup> *Physics and Astronomy, University of Exeter, Stocker Road, Exeter EX4 4QL, England*

<sup>4</sup> *Department of Physics, University of Alberta, 4-181 CCIS Edmonton AB T6G 2E1, Canada*

<sup>5</sup> *Jeremiah Horrocks Institute, University of Central Lancashire, Preston, Lancashire, PR1 2HE, England*

<sup>6</sup> *National Research Council Canada, 5071 West Saanich Road, Victoria, BC, V9E 2E7, Canada*

<sup>7</sup> *Astrophysics Group, Cavendish Laboratory, J J Thomson Avenue, Cambridge CB3 0HE, England;*

<sup>8</sup> *Astrophysics Research Institute, Liverpool John Moores University, Birkenhead, Wirral, CH41 1LD, England*

<sup>9</sup> *Joint Astronomy Centre, 660 N. A'ohoku Place, University Park, Hilo, Hawaii 96720, USA*

<sup>10</sup> *Kapteyn Astronomical Institute, Postbus 800, 9700 AV, Groningen, Holland*

<sup>11</sup> *Imperial College, Blackett Laboratory, Prince Consort Road, London SW7 2AZ, England*

<sup>12</sup> *National Research Council Canada, 5071 West Saanich Rd, Victoria, BC, V9E 2E7, Canada*

<sup>13</sup> *Leiden Observatory, Leiden University, PO Box 9513, 2300 RA, The Netherlands*

<sup>14</sup> *Dunlap Institute for Astronomy & Astrophysics, University of Toronto, 50 St. George St., Toronto, ON, M5S 3H4, Canada*

<sup>15</sup> *Department of Physics and Astronomy, University of Victoria, Victoria, BC, V8P 1A1, Canada*

2 October 2018

## ABSTRACT

CO,  $^{13}\text{CO}$  and  $\text{C}^{18}\text{O}$   $J = 3-2$  observations are presented of the Ophiuchus molecular cloud. The  $^{13}\text{CO}$  and  $\text{C}^{18}\text{O}$  emission is dominated by the Oph A clump, and the Oph B1, B2, C, E, F and J regions. The optically thin(ner)  $\text{C}^{18}\text{O}$  line is used as a column density tracer, from which the gravitational binding energy is estimated to be  $4.5 \times 10^{39}$  J ( $2282 M_{\odot} \text{ km}^2 \text{ s}^{-2}$ ). The turbulent kinetic energy is  $6.3 \times 10^{38}$  J ( $320 M_{\odot} \text{ km}^2 \text{ s}^{-2}$ ), or 7 times less than this, and therefore the Oph cloud as a whole is gravitationally bound. Thirty protostars were searched for high velocity gas, with eight showing outflows, and twenty more having evidence of high velocity gas along their lines-of-sight. The total outflow kinetic energy is  $1.3 \times 10^{38}$  J ( $67 M_{\odot} \text{ km}^2 \text{ s}^{-2}$ ), corresponding to 21% of the cloud's turbulent kinetic energy. Although turbulent injection by outflows is significant, but does *not* appear to be the dominant source of turbulence in the cloud. 105 dense molecular clumplets were identified, which had radii  $\sim 0.01-0.05$  pc, virial masses  $\sim 0.1-12 M_{\odot}$ , luminosities  $\sim 0.001-0.1 \text{ K km s}^{-1} \text{ pc}^{-2}$ , and excitation temperatures  $\sim 10-50\text{K}$ . These are consistent with the standard GMC based size-line width relationships, showing that the scaling laws extend down to size scales of hundredths of a parsec, and to sub solar-mass condensations. There is however no compelling evidence that the majority of clumplets are undergoing free-fall collapse, nor that they are pressure confined.

**Key words:** stars: formation - molecular data - ISM: kinematics and dynamics - submillimetre - ISM: jets and outflows

## 1 INTRODUCTION

The Gould Belt survey is a Legacy programme that uses the James Clerk Maxwell telescope (JCMT) to map the dust and

gas distributions in nearby star forming molecular clouds (Ward-Thompson et al. 2007). Tilted  $\sim 20$  degrees from the Galactic Plane, the Gould Belt contains many of the closest low and high-mass star forming regions and OB associations. This geometry allows many of these regions to be studied at high spatial resolution, and with relatively little confusion by foreground or background Galactic emission. The goal of the present study is to map the CO,  $^{13}\text{CO}$  and  $\text{C}^{18}\text{O}$   $J = 3-2$  distributions from the Ophiuchus Molecular cloud. Studies of other targets in the JCMT Gould Belt survey have already been presented: Orion A (Buckle et al. 2012), Orion B (Buckle et al. 2010), Serpens (Graves et al. 2010), Taurus (Davis et al. 2010), and in Perseus (Curtis et al. 2010).

The paper is organised as follows: Section 2 describes the overall Ophiuchus Cloud and previous observations, Section 3 reports the observational and instrumentation characteristics, Section 4 presents the observational data and analyses the excitation temperatures, opacities of the gas and cloud, Section 5 determines the characteristics of the outflows and their analyses their impact on the global kinematics of the cloud, Section 6 gives the properties of the small scale structure (clumplets) across the mapped region, and Section 7 summarising the results of this study.

## 2 THE OPHIUCHUS CLOUD

Located  $120 \pm 5$  pc from the sun (Loinard et al. 2008, Lombardi, Lada & Alves 2008), the Ophiuchus cloud is one of the closest low-intermediate mass star forming regions (Motte et al. 1998, Johnstone et al. 2000, Padgett et al. 2008, Miville-Déschenes et al. 2010). It is dominated by the main Oph A clump, also known as LDN (Lynds Dark Nebula) 1688. The line of sight extinction  $A_V \sim 50-100$  mag (Wilking & Lada 1983, Khanzadyan et al. 2004).

CO isotopic measurements have previously been reported by White et al. (1986), Ladd (2004), Wouterloot, Brand & Henkel (2005), Minchin & White (1995) and White & Sandell (1995). A large atomic carbon, CI, and CO map of the Ophiuchus cloud has been presented by Kamegai et al. (2003), and extensive  $^{13}\text{CO}$  measurements reported by Loren (1989a,b, 1990). Other molecular line observations have included  $\text{HCO}^+$ ,  $\text{NH}_3$ , [OI],  $\text{NH}_3$  by Boogert et al. (2002),  $\text{O}_2$  by Larsson et al. (2007), Liseau & Justtanont (2009), Liseau et al. (2012) and Maruta et al. (2010),  $\text{H}_2\text{D}^+$  by Harju et al. (2008),  $\text{H}_2\text{O}$  by Imai et al. (2007),  $\text{NH}_3$  by Friesen et al. (2009), CI (Kulesa et al. 2005), and in the far-IR continuum (Ceccarelli et al. 1998, Liseau et al. 1999a).

A bright filament of far-IR emission traces the western edge of the molecular clump, and appears associated with an edge-on photodissociation region close to HD 147889 (Liseau et al. 1999a; Kulesa et al. 2005, Cassassus et al. 2008). Such filamentary structures are widely recognised as being associated with star forming molecular cores (Palmerin et al. 2013). Mapping of the [CI] and [CII] lines show that these lines primarily trace emission from the lower density envelopes of molecular clumps illuminated from the far side of the cloud (Kamegai et al. 2003; Kulesa et al. 2005). This emission follows the column density distribution of the molecular gas and is modelled as having temperatures of 50–200 K, surrounded by lower temperature gas at  $\sim 20$  K (Kulesa et al. 2005).

The early stages of star formation can be studied by observations of the outflows and/or jets from embedded objects, usually from CO or  $\text{H}_2$  imaging (Phillips et al. 1982, White et al. 2000, Beckford et al. 2008, Nakamura et al. 2011). Previous surveys of the Ophiuchus cloud complex at millimetre, infrared and optical wavelengths have led to the identification of a number of CO molecular outflows (Loren 1989a,b, André et al. 1990, Zhang & Wang 2009, van der Marel et al. 2013, Hatchell et al. 2012), as well as individual outflows associated with IRS 44 (Terebey et al. 1989); VLA 1623 (André et al. 1990, Dent et al. 1995); GSS 30 (Tamura et al. 1990); Oph B (Kamazaki et al. 2003) and the ELIAS12/VLA 1623 region (Dent, Matthews & Walther 1995, Narayanan & Logan 2006, Bussman et al. 2007), which are covered by the present observations.

Atomic jets and Herbig-Haro (HH) objects have also been discovered in the cloud (Wilking et al. 1997, Gómez et al. 1998, 2003, Phelps & Barsony 2004, Wu et al. 2002, Smith et al. 2005). Near-infrared ( $\text{H}_2$  2.12  $\mu\text{m}$ ) imaging observations have been used to identify shock-excited knots and jets located toward highly obscured areas (Davis & Eisloffel 1995; Dent et al. 1995; Molinari et al. 2000; Davis et al. 2010; Grosso et al. 2001, Habart et al. 2010, 2011, Zhang et al. 2013). *Spitzer* maps of the region have been reported by Lombardi, Lada & Alves (2008), and radio continuum observations by Casassus et al. (2008) and Loinard et al. (2007). The distribution of pre-stellar clumps and YSOs has been presented by Ratzka et al. (2005), Smith et al. (2005), Young et al. (2006), Stamatellos, Whitworth & Ward-Thompson (2007), Jørgensen et al. (2008), Enoch et al. (2008), Padgett et al. (2008). The turbulent nature and motions of the gas have been studied by Snow, Destree & Welty (2008), Schmeja, Kumar & Ferreira (2008) and Friesen et al. (2009).

The radiation field in LDN 1688 is dominated by two embedded B-type double stars,  $\rho$  Oph AB, which are located at a distance of  $110_{-10}^{+12}$  pc, and have spectral classes B2V+B2V (Abergel et al. 1996, Cassassus et al. 2008, Rawlings et al. 2013). These have a combined luminosity  $L = 5800 L_{\odot}$ , with the other double system, HD 147889 at a distance of  $118_{-11}^{+12}$  pc, and stars with spectral classes B2IV+B3IV and  $L = 7800 L_{\odot}$  (Rawlings et al. 2013). HD 147889, is located 0.5–1 pc away from the far side of the Oph A clump. The UV-field is about 1 per cent of that of the well studied Orion Bar (White et al. 2003, Liseau et al. 1999a,b, Habart et al. 2003, Naylor et al. 2010, Buckle et al. 2012, Arab et al. 2012, Bernard-Salas et al. 2012). However, the interstellar dust in Ophiuchus shows unusual dust extinction properties, with components due to large dust grains (Chapman et al. 2009), and very small, rapidly rotating grains (Cassassus et al. 2008, Dickinson et al. 2009, Castellanos et al. 2011). This dust will significantly mask UV radiation resulting from star forming activity. Other early-type stars in the Upper Scorpius OB Association may also have deposited energy into the cloud (Greene & Meyer 1995, Thompson et al. 2004, Luhman & Rieke 1999, Ratzka, Köhler & Leinert 2005, Zavagno et al. 2010).

Although most of the condensed objects appear to be relatively old T-Tauri stars, at least six major areas undergoing active star-formation have been identified: Oph-A to Oph-F respectively, which contain many pre-stellar clumps and Young Stellar Objects (YSOs) (Loren, Woot-

ten, & Wilking 1990, Allen et al. 2002, Ridge et al. 2006, Friesen et al. 2009, van Kempen et al. 2009). The most active star-forming part of the Ophiuchus complex, LDN 1688, contains almost half of the mass of the Ophiuchus cloud, and exhibits a relatively high gas-star conversion efficiency that has been estimated to be  $\sim 22$  per cent (Wilking, Lada & Young 1989). The Oph B region is the second densest clump in the Ophiuchus cloud complex, containing several 1.3 mm dust continuum sources (André, Ward-Thompson & Barsony 1993, Motte, André, & Neri 1998, Liseau, White & Larsson 1999b, Jørgensen et al. 2008), which are likely to be very young protostars.

The above description has focussed on previous studies relevant to this paper, for more extensive details of other studies of the Ophiuchus region, the reader is referred to the compilation by Wilking, Gagne & Allen (2008).

### 3 THE OBSERVATIONS

#### 3.1 JCMT observations

The HARP (Heterodyne Array Receiver Programme - see Buckle et al. 2009) receiver contains an array of 16 heterodyne detectors, arranged in a  $4 \times 4$  footprint on the sky. HARP was used to make maps in the CO,  $^{13}\text{CO}$  and  $\text{C}^{18}\text{O}$   $J = 3-2$  lines, where it has a beamsize of  $14''$  at 345 GHz (corresponding to a linear size of 0.008 pc at the Ophiuchus cloud).

The HARP receptors were operated as single sideband detectors, with system noise temperatures  $T_{\text{sys}} \sim 350-500$  K for the various lines. The main-beam efficiency was taken from the JCMT efficiency archive, and assumed to be  $\eta_{mb} = 0.61$  at 345 GHz; with the values of the forward coupling efficiency,  $\eta_{fss} = 0.71, 0.72$  and  $0.78$  at 329, 330 and 345 GHz respectively<sup>1</sup>. In general, the data presented in this paper are in units of main beam brightness temperature  $T_{mb}$  (Kutner & Ulich 1981) unless otherwise stated in the text, although appropriate beam efficiency corrections were made (usually to main beam brightness temperature when discussing the compact clumps) to estimate the properties of the gas, as discussed in later sections of this paper.

The molecular line observations were made up of 3.2 hours of CO data taken in February and March 2008 and 16.6 hours of  $^{13}\text{CO}$  and  $\text{C}^{18}\text{O}$  observations taken during March, July, and August 2008. The maps were observed using the standard on-the-fly mapping mode, and referenced against an off-source reference position at RA(J2000) =  $16^{\text{h}} 38^{\text{m}} 00.6^{\text{s}}$ , Dec(J2000) =  $-25^{\circ} 36' 42.0''$ , which had been verified to show no line emission from examination of 60 second position-switched ‘stare’ observation in CO. The CO data were taken with the AutoCorrelation Spectrometer and Imaging System (ACSIS) using its 250 MHz dual sub-band mode that provided 4096 channels, each with a velocity resolution  $\sim 0.05$  km s<sup>-1</sup> per channel. The  $^{13}\text{CO}/\text{C}^{18}\text{O}$  data were taken simultaneously with each other, with each sub-band having a central rest frequency of 330.587 or 329.330 GHz respectively, providing a velocity resolution  $\sim 0.055$

Region	CO $T_{mb}$ K	$^{13}\text{CO}$ $T_{mb}$ K	$\text{C}^{18}\text{O}$ $T_{mb}$ K
Oph B-F	0.13	0.08	0.08
Oph A	0.19	0.14	0.11
Map edges	0.32	0.19	0.21

**Table 1.** The rms main beam brightness temperature noise levels for a  $0.1$  km s<sup>-1</sup> wide velocity channel in various areas of the Ophiuchus cloud for each of the isotopologues are reported in this Table.

km s<sup>-1</sup>. All of the isotopologue maps were then further convolved to a resolution of  $0.1$  km s<sup>-1</sup>.

To smooth out noise variations due to missing receptors or differences in receptor performance, two independent maps were made by scanning in orthogonal directions (a technique known as ‘basket-weaving’), which helps to mitigate scanning effects due to systematic zero level offsets between adjacent detector scans. To remove some remaining low level striping effects, the data cubes were searched for artefacts using a  $3-\sigma$  clipped image mask in each velocity channel, followed by use of a Hough transform to search for residual linear features in the data that might be indicative of such scanning artefacts aligned along the array scan direction. This destriping correction typically corresponded to cosmetic changes at the  $\sim 1-2$  per cent of the peak brightness level of the map at a given point, and did not quantitatively alter the results reported here, except in a cosmetic way.

#### 3.2 UKIRT observations

To support the JCMT observations, a deep United Kingdom Infrared Telescope (UKIRT) image of the Oph region was obtained using a near-IR K-band filter, and a matching narrow-band H<sub>2</sub> image. This was used to observe the H<sub>2</sub> 2.122  $\mu\text{m}$   $v = 1-0$   $S(1)$  vibrationally excited line at 2.122  $\mu\text{m}$  line, which is excited in high temperature gas of several hundred up to several thousand K, and traces shocked and/or fluorescently excited material in PDRs (White et al. 1987, 2000, Davis & Eisloffel 1995, Wilking et al. 1997, Gómez et al. 1998, Dent et al. 1995, Grosso et al. 2001). Narrow band H<sub>2</sub> images were obtained with UKIRT during June 2010 using the near-IR wide-field camera WFCAM. This contained four Rockwell Hawaii-II (HgCdTe 2048  $\times$  2048) arrays giving an effective pixel size of  $0.4''$ . Observations at four pointing positions were dithered and mosaiced together. At each of these four positions, eight exposures were obtained, each with 20 seconds integration time in the H<sub>2</sub> line, and 5 seconds in the nearby K-band continuum. The images were shifted by an integral multiple of  $0.2''$  to give a final pixel scale of  $0.2''$ . The residual sky/background structure was removed by fitting a coarse surface to each image (as described by Davis et al. 2010). In the final step, the broad band K-band (continuum) image was aligned with the same frame as the H<sub>2</sub> exposure, scaled and subtracted. On the final image some stars appear as negative (black) spots (due to imperfect subtraction), although regions showing diffuse emission are recovered well. Many H<sub>2</sub> emission clumps from the Ophiuchus Molecular Hydro-

<sup>1</sup> The  $\text{C}^{18}\text{O}$ ,  $^{13}\text{CO}$  and CO  $J = 3-2$  rest frequencies were 329.3305525, 330.5879601 and 345.7959899 GHz respectively.

gen Emission-Line Objects (MHOs) reported by Davis et al. (2010), that were not initially visible on the UKIRT K-band continuum image, were successfully recovered using this technique, along with a number of previously uncatalogued objects. The H<sub>2</sub> image will be used later in this paper in Figures 9, 11 and 13.

#### 4 CLOUD STRUCTURE AND PHYSICAL PROPERTIES

For consistency throughout this paper, four kinds of cloud structure will be referred to: ‘cloud’, meaning the overall Ophiuchus Cloud that has been observed (overall size  $\sim$  several pc); ‘clumps’, meaning individual condensations, such as Oph A, Oph B etc. with typical sizes  $\sim$  0.05–0.2 pc; sub-structures of the clumps which we call ‘clumplets’, which refer to the smallest scale structures recovered in Section 6 from the 3-dimensional (RA, Dec, velocity) data cube, and which have typical sizes of up to  $\sim$ 0.05 pc; and ‘prestellar cores’, which are gravitationally bound starless cores within the cloud, which are detected by the presence of thermal continuum emission (at 1300 or 850  $\mu$ m). The last of these is introduced because the stability/longevity of the clumplet structures is currently uncertain (see Section 6), and they need to be distinguished compared to the more commonly used terminology of ‘clumps’ that feature in many other studies. The large scale integrated CO emission across the region covering Oph A and Oph B, C, E, F, and J clumps is shown in Fig 1, along with the SCUBA 850  $\mu$ m image from Johnstone et al. (2000).

The CO map is dominated by bright emission from the Oph A region, which is itself fragmented into an hierarchy of smaller clumps. The CO map also shows the prominent curved molecular outflow that extends for  $\sim$  30’ ( $\sim$ 1 pc) away from the well studied source VLA 1623. Away from Oph A many other molecular clumps are visible, which show some correlation to the 850  $\mu$ m submm continuum maps shown on the same scale. Although the <sup>13</sup>CO and C<sup>18</sup>O integrated emission maps cover a smaller area than that of the CO image, they show that the isotopologues are strongly concentrated around the Oph A region, but again that many small clumps are well correlated with enhancements on the CO map, including all of those identified on the 850  $\mu$ m map. Comparison with the integrated CO distribution needs to be treated with caution as many of the CO (and <sup>13</sup>CO) lines are strongly self-absorbed by foreground emission.

The large scale CO channel maps are shown in Fig 2. CO emission is present over a wide velocity range in excess of 12 km s<sup>-1</sup>. From the C<sup>18</sup>O observations (see Fig. 4), The systemic velocity,  $v_{lsr}$  of the cloud, lies mostly between  $\sim$  2 and 4 km s<sup>-1</sup>, with typical C<sup>18</sup>O half power linewidths  $\sim$  1.5 km s<sup>-1</sup>. The CO emission by contrast extends over the velocity range  $-3 \rightarrow +8$  km s<sup>-1</sup>, with much of the gas at the higher offsets from the systemic velocity (taken from the C<sup>18</sup>O spectra) being associated with molecular outflows. At the most blueshifted offset velocities, the maps are dominated by emission from the Oph B2 region, and from the VLA 1623 outflow jet, the latter being seen most clearly in the +1 km s<sup>-1</sup> map. Bright emission from the Oph A clump region dominates at a velocity of  $\sim$  +2 km s<sup>-1</sup>, but at velocities redshifted from  $\sim$  +4 km s<sup>-1</sup> the channel map

shows little structure, particularly to the south-east of the Oph A clump, which is a consequence of the very deep self-absorption by foreground material at this velocity. At  $v_{lsr}$  velocities between +5 and +8 km s<sup>-1</sup> the distribution contains a lot of small-scale structure not seen in the CO maps.

The large scale <sup>13</sup>CO channel maps are shown in Fig 3. The <sup>13</sup>CO emission is seen between 0 and +7 km s<sup>-1</sup>. As with the CO channel maps, the <sup>13</sup>CO map fails to show prominent bright small scale structure to the south-east Oph A region, even though this area contains a number of prominent submm sources. Again, this is probably a consequence of wide-spread self-absorption.

The large scale C<sup>18</sup>O channel maps are shown in Fig 4. It is clear that in the velocity channels where (particularly toward the Oph A region) the CO is strongly affected by self-absorption, the C<sup>18</sup>O channel maps show more small-scale structure, and appear to better trace the distribution of the denser material and gas clumps in the cloud. The general spatial structure from the JCMT map agrees well with that presented by Liseau et al. (2010), who have mapped the C<sup>18</sup>O  $J = 3-2$  line from an  $\sim 10' \times 5'$  area centred on the Oph A clump using the APEX telescope.

Overlays of the data with other tracers of star formation are given in Figure 5.

#### 4.1 Excitation temperatures

Assuming that CO and <sup>13</sup>CO are optically thick, excitation temperatures  $T_{ex}$  can be determined from  $T_{mb}$  using Equation 1:

$$T_{ex} = \frac{h\nu}{k} \left[ \ln \left( \frac{h\nu/k}{T_{mb} + J_\nu(T_{bg})} + 1 \right) \right]^{-1} \quad (1)$$

where  $T_{bg} = 2.73$  K is the microwave background temperature and  $J_\nu(T)$  is as defined in Equation 2:

$$J_\nu(T) = \frac{h\nu}{k} \frac{1}{e^{(h\nu/kT)} - 1} \quad (2)$$

In the Ophiuchus cloud the CO lines of the main cloud components often appear self-absorbed and cannot always reliably be used to estimate the excitation temperature, as foreground absorption by cooler gas reduces the main beam antenna temperatures. In cases where the <sup>13</sup>CO line is optically thick, it has been used in place of the CO line (Christie et al. 2012). The Ophiuchus region presents an exceptional case, such that even in the rare <sup>13</sup>C<sup>18</sup>O isotope, the lines towards some of the denser clumps also appear opaque (Liseau et al. 2010).

Examples of typical spectra representative of the data quality from the Oph region are shown in Fig 6. These spectra show how the spectral appearance changes amongst the various isotopologues, which is due to the widespread self-absorption that is seen throughout the cloud.

The excitation temperatures for CO and <sup>13</sup>CO estimated from the data are shown in Figure 7. There are strong absorption features in the CO emission ranging from  $\sim$  2.0–5.5 km s<sup>-1</sup> and it is possible the excitation temperature has been underestimated for this transition. From past studies, excitation temperatures are often observed to rise in protostellar outflows (Phillips et al. 1982, 1988, Rainey et al. 1987, Hatchell et al. 1999a, Nisini et al. 2000, Giannini et al. 2001).

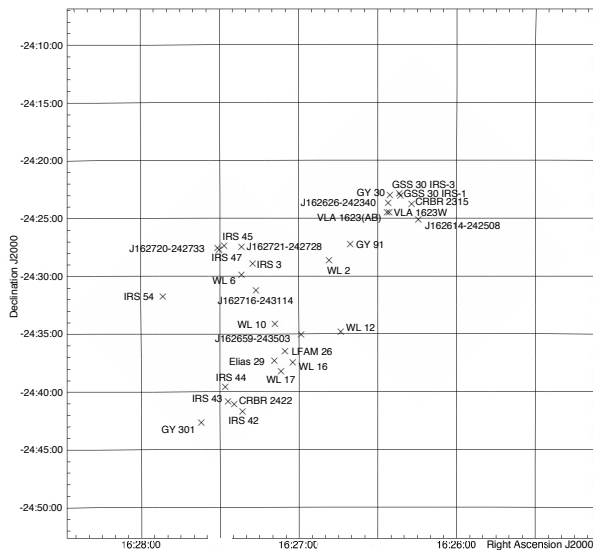
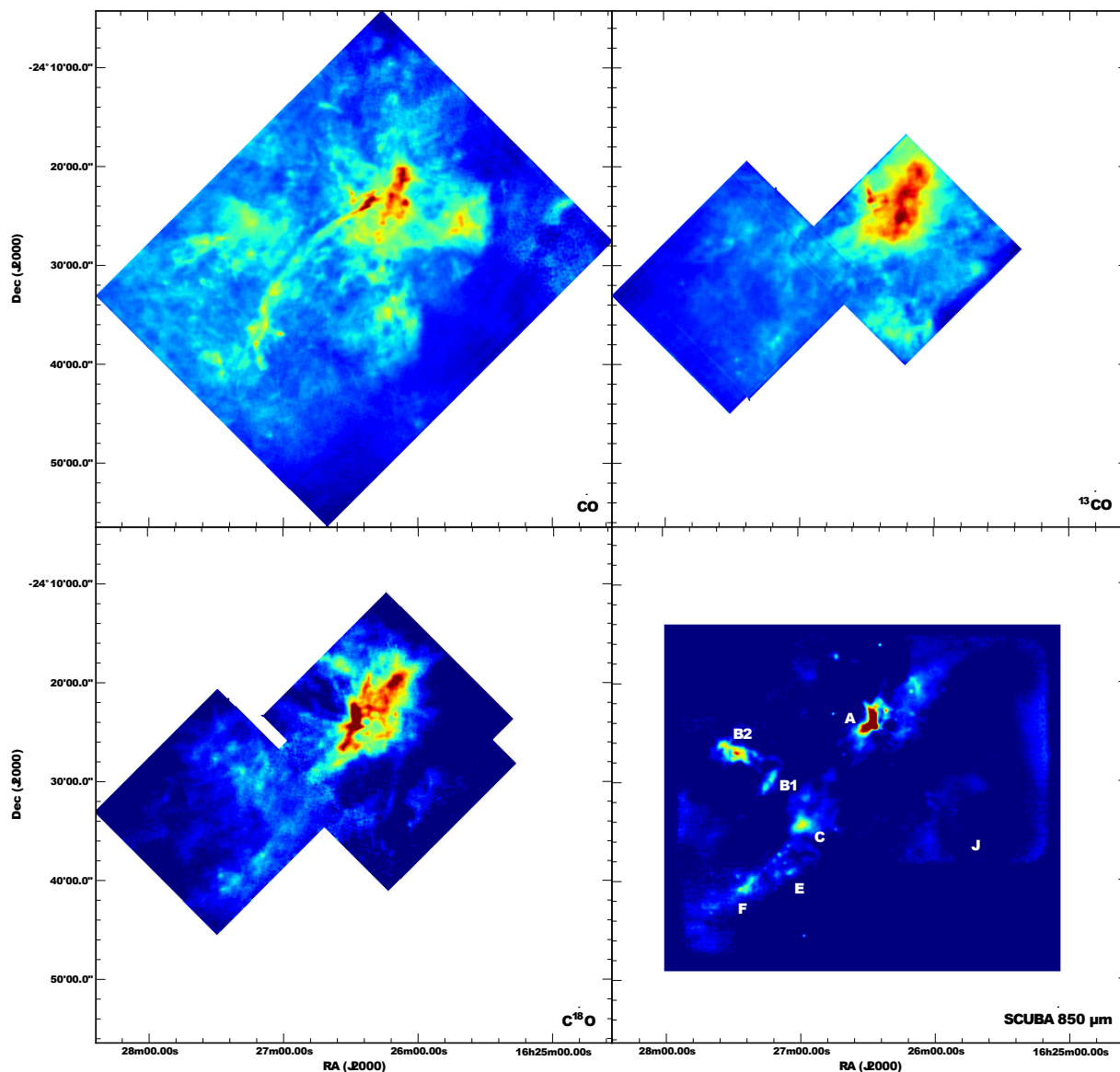


**Figure 1.** [Upper] CO  $J = 3-2$  observations [top left] showing the integrated emission between  $-5$  and  $+12$  km s $^{-1}$ ; [top right]  $^{13}\text{CO}$  emission between  $0$  and  $+7$  km s $^{-1}$ ; [lower left]  $\text{C}^{18}\text{O}$  emission between  $0$  and  $+7$  km s $^{-1}$  and [lower right] the SCUBA  $850\ \mu\text{m}$  image from Johnstone et al. (2000). The maximum value in the CO  $J = 3-2$  map is  $T_{mb} = 105$  K km s $^{-1}$  close to the Oph A clump. [Lower] Orientation map showing the locations of sources referred to in the text, and in Table 2.

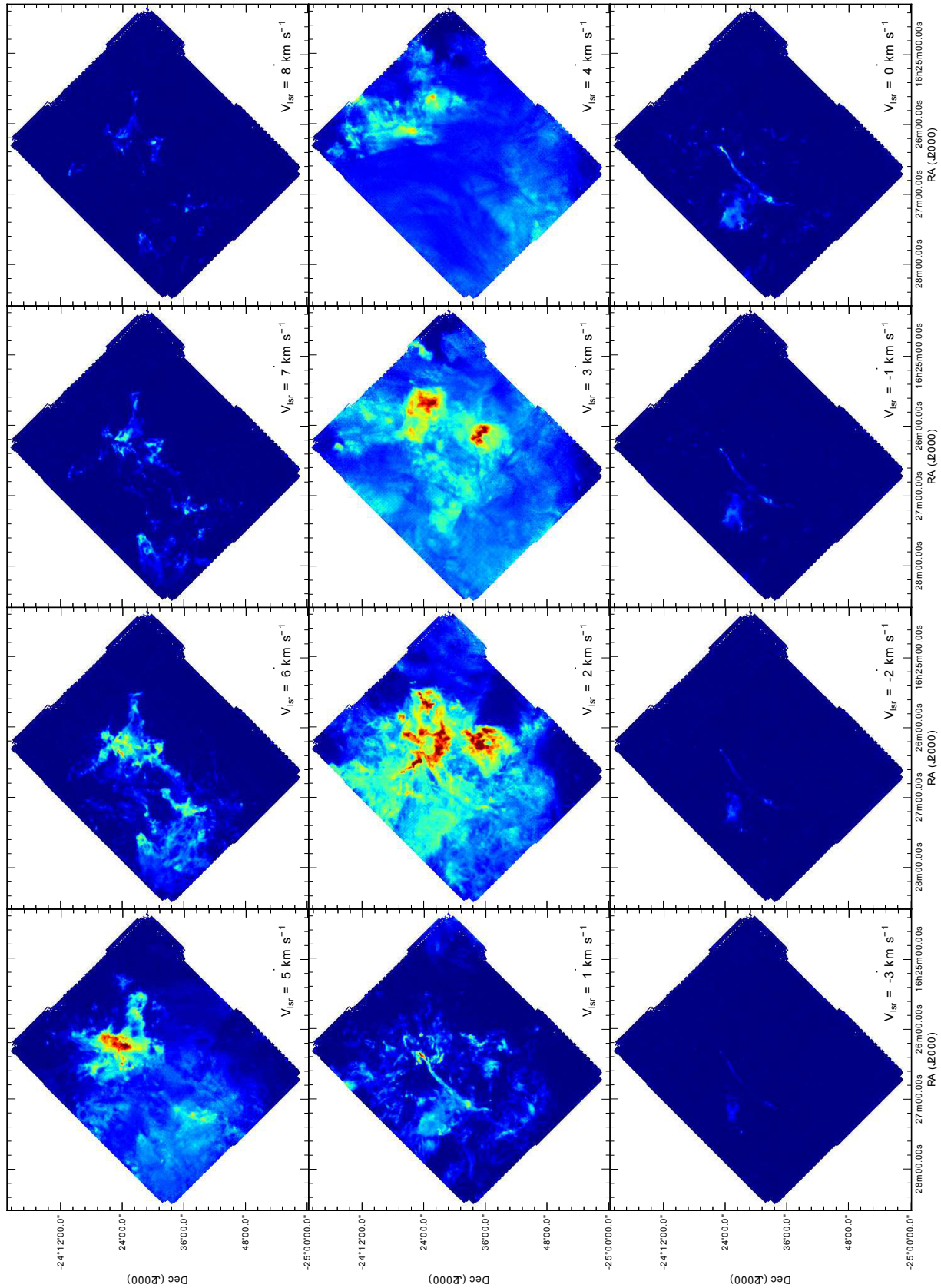


**Figure 2.** CO  $J = 3-2$  map in  $1 \text{ km s}^{-1}$  velocity channel maps. Oph A is in the upper right hand part of the figure, and the Oph D clumps are in the lower left part of the figure. The colour scaling is shown linearly between  $T_{mb} = 0$  and  $58 \text{ K}$ .

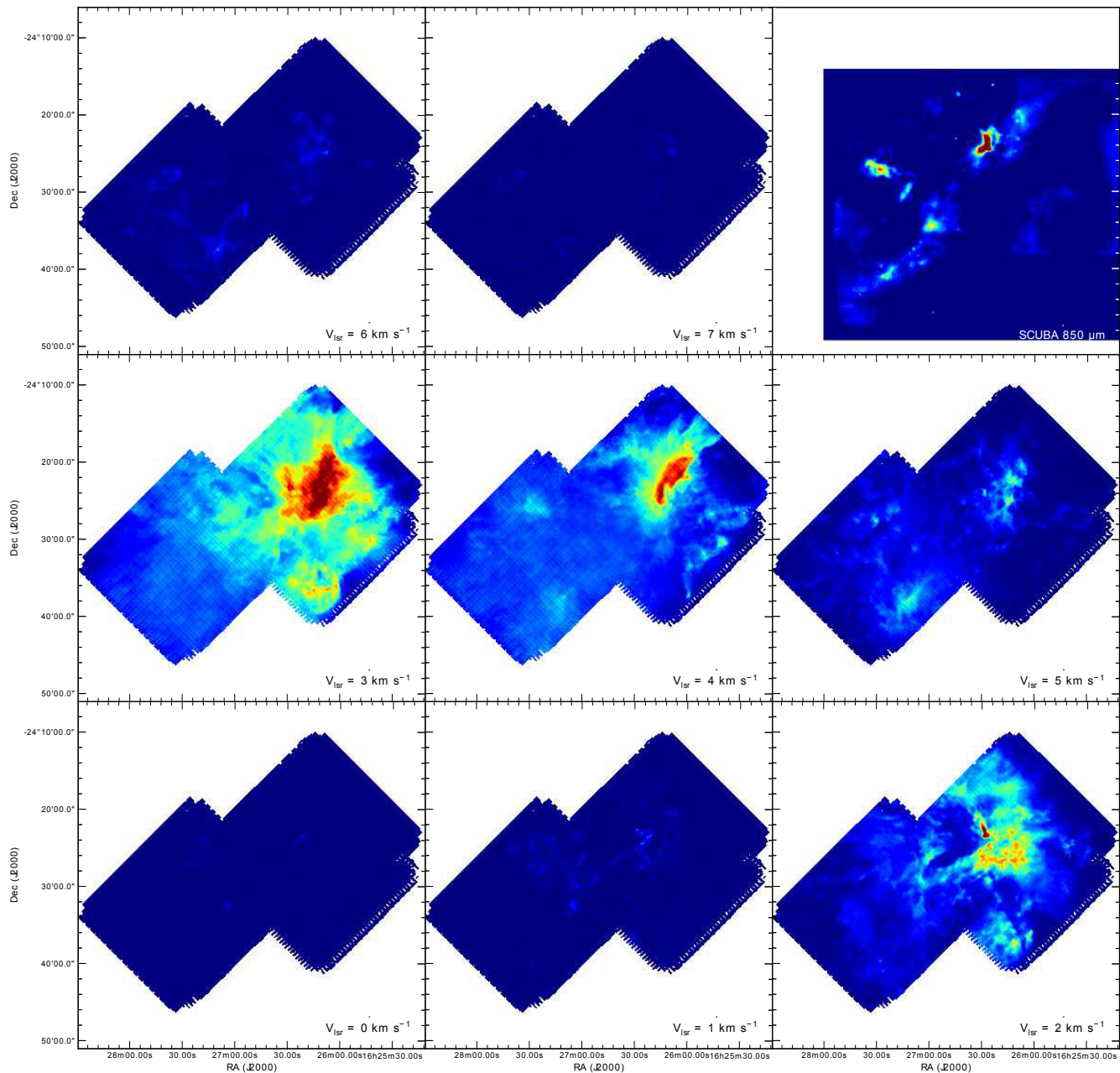


**Figure 3.** The  $^{13}\text{CO } J = 3-2$  emission between 0 (top right) and +8 (bottom left)  $\text{km s}^{-1}$ . The highest value is  $T_{mb} = 21 \text{ K km s}^{-1}$  in a  $1 \text{ K km s}^{-1}$  channel close to the Oph A clump. The  $850 \mu\text{m}$  map is shown again as a position reference.

Throughout the cloud,  $T_{\text{ex}}(\text{CO})$  and  $T_{\text{ex}}(^{13}\text{CO})$  are typically between  $\sim 12\text{--}40 \text{ K}$ .

A noticeable feature in the maps is the warm gas tracing the PDR close to Oph J that is illuminated by the early-type B-type stars S1 and SR3 and (mostly from) the close binary HD 147889 (B2IV, B3IV; Cassassus et al. 2008), as shown in Figure 2. The excitation temperatures near to the PDR reach  $\sim 80 \text{ K}$  for CO and  $\sim 50 \text{ K}$  for  $^{13}\text{CO}$ . These excitation temperatures are significantly higher than temperatures found inferred for many of the regions with molecular outflows. For example near the VLA 1623 outflow in Oph A, CO excitation temperatures reach  $30\text{--}40 \text{ K}$  in the blueshifted flow and higher in the redshifted flow ( $40\text{--}50 \text{ K}$ ), close to

the PDR. The Elias 32 and WL 6 outflows in Oph B (see Section 5.2) have CO excitation temperatures ranging from  $20\text{--}30 \text{ K}$ , which are similar to the temperatures found in the flows from Oph C, E, and F (including Elias 29, WL 10, IRS 44, and IRS 43 - see Sections 5.3 and 5.4).

The excitation temperatures for  $^{13}\text{CO}$  appear noticeably lower than that of CO even though the CO emission is affected by self absorption. This suggests that  $^{13}\text{CO}$  may be optically thin in some regions, and that temperature estimates based on this line should therefore be corrected to take account of this.

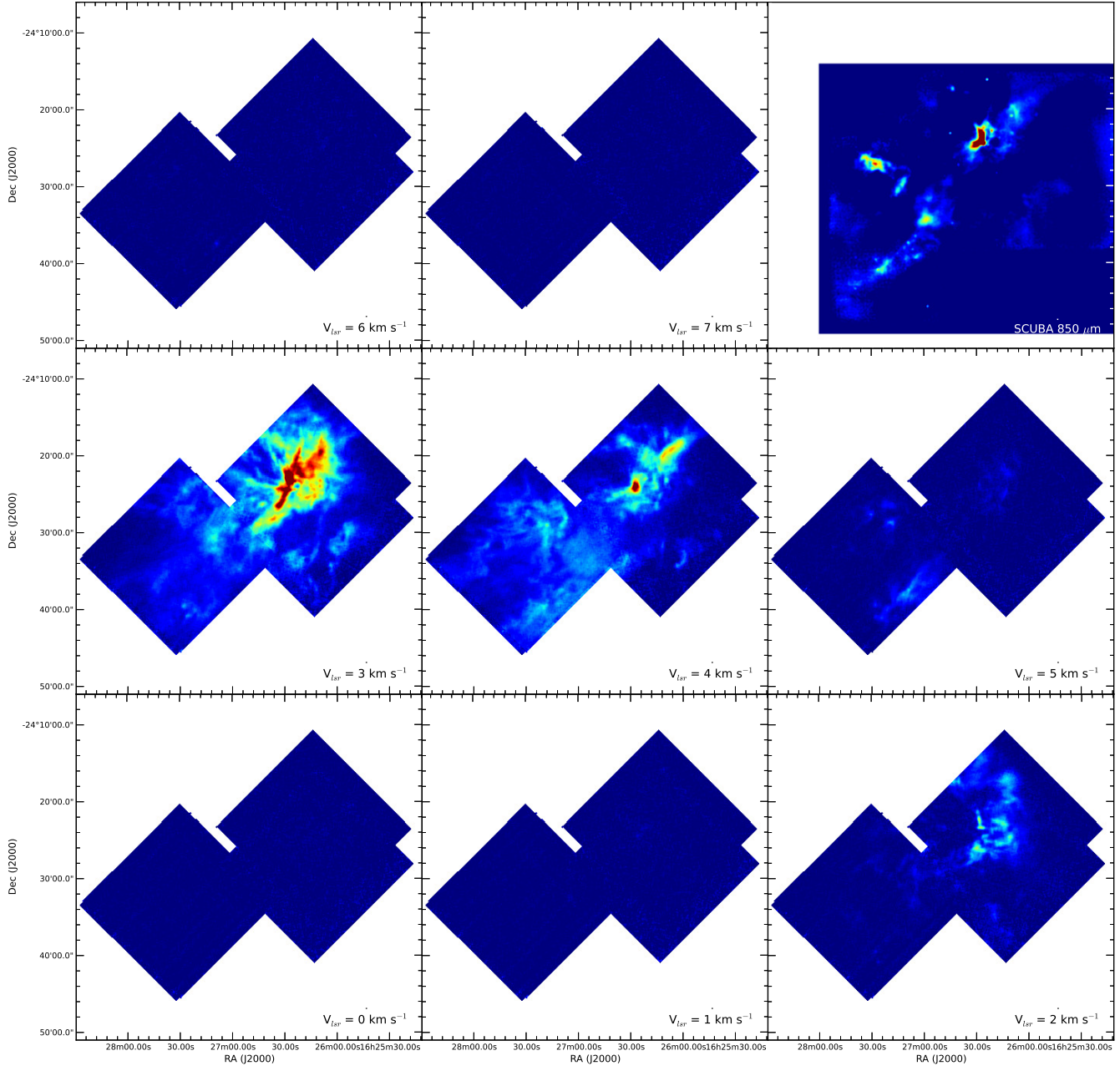


**Figure 4.** The  $C^{18}O$   $J = 3-2$  emission between 0 (top right) and +8 (bottom left)  $\text{km s}^{-1}$ . The highest value is  $10.6 \text{ K km s}^{-1}$  in a  $1 \text{ K km s}^{-1}$  channel close to the Oph A clump.

## 4.2 Opacities in the main clumps

In this section, the data are used to infer the optical depth of  $^{13}\text{CO}$  or  $C^{18}O$  in the cloud, and from this the mass of the cloud components. For this it is assumed that the optically thinner  $C^{18}O$  can be used to trace the column density and mass in the cloud. However in a region like this suffering high extinction, it is important to confirm whether the emission is in fact optically thin. Following Equation 8 the optical depth is related to the intensity ratio of different CO isotopologues,  $I(^{13}\text{CO})/I(C^{18}O)$ , by the relation,

$$\frac{T_{13\text{CO}}}{T_{C^{18}O}} = \frac{1 - \exp(-\tau(^{13}\text{CO}))}{1 - \exp(-\tau(C^{18}O))} \quad (3)$$

where  $T$  is the brightness temperature and  $\tau$  is the optical depth (of the corresponding subscripted isotopologues). Using the method in Ladd, Fuller & Deane (1998), the ratio of  $^{13}\text{CO}$  and  $C^{18}O$  integrated intensities can be used together to provide an estimate of the optical depth of the cloud:

$$\frac{\int_{-\infty}^{\infty} T_{13\text{CO}}(v) dv}{\int_{-\infty}^{\infty} T_{C^{18}O}(v) dv} = \frac{\int_{-\infty}^{\infty} (1 - \exp[-\tau_{13\text{CO}}(v)]) dv}{\int_{-\infty}^{\infty} (1 - \exp[-\tau_{C^{18}O}(v)]) dv} \quad (4)$$

where  $\tau(C^{18}O) = \tau(^{13}\text{CO})/f_{18}$ , with  $f_{18}$  representing the abundance ratio  $^{13}\text{CO}/C^{18}O$ . This equation can be further simplified by setting  $\tau(^{13}\text{CO}) = \tau(^{13}\text{CO}) \exp[-v^2/2\sigma^2]$ , which assumes a Gaussian velocity

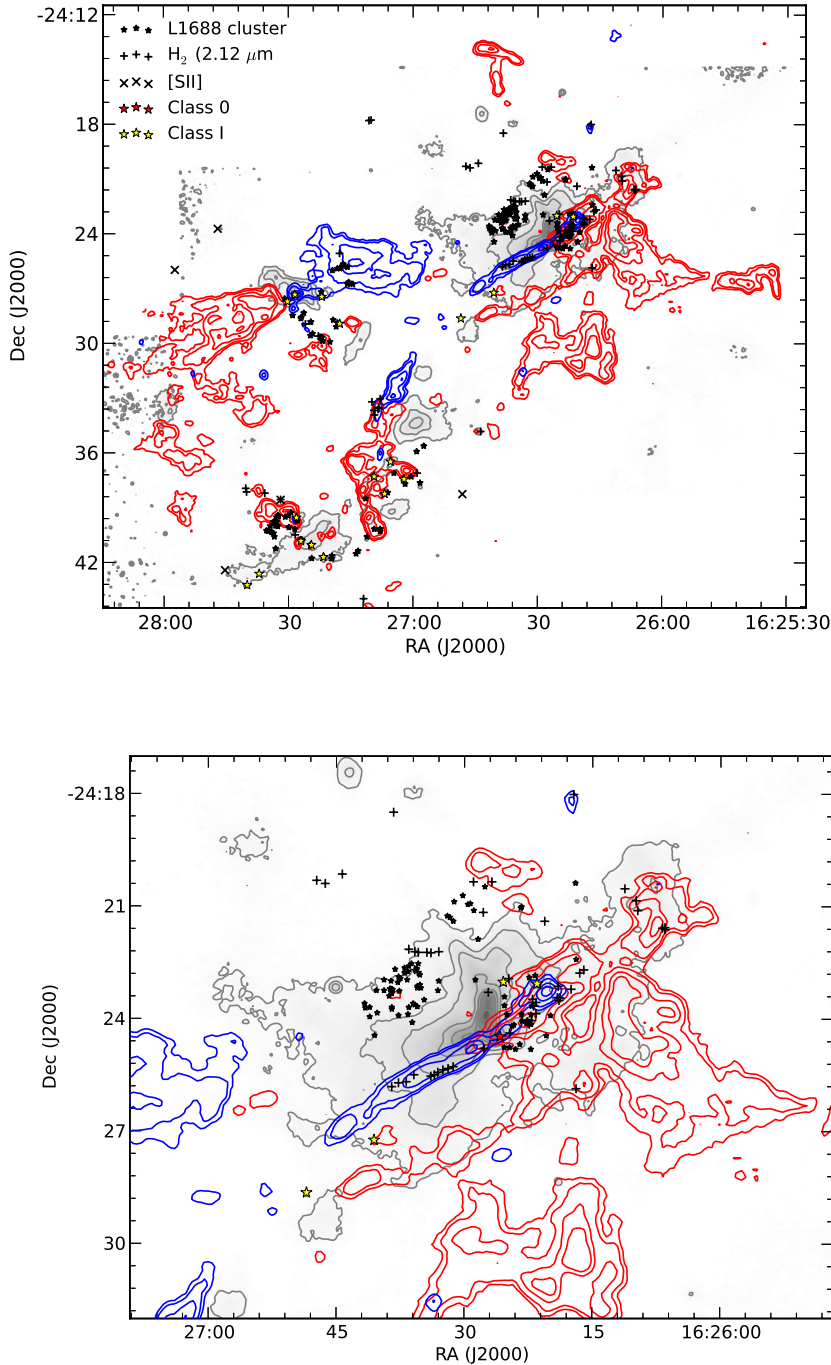


**Figure 5.** [Upper] Comparison between the JCMT CO data and other observations for the cloud; [Lower] Zoom-in on the Oph A clump. In both panels the blue and red outflows are appropriately colour coded, which the contour levels are arbitrarily chosen to emphasise the outflows. Blue contours are integrated from  $-8.6$ – $0.4$   $\text{km s}^{-1}$  and red contours are integrated from  $6.4$ – $15.4$   $\text{km s}^{-1}$ . For both maps the contour levels are at  $T_{\text{mb}} = 3, 5, 10, 15, 30,$  and  $45$   $\text{K km s}^{-1}$ . The annotations are from the following sources: L1688 cluster: Allen et al. 2002 NICMOS,  $\text{H}_2$  shocks and [SII]: Gomez et al. 2003  $2.12 \mu\text{m}$  data; Class 0/I protostars: Enoch et al. 2009 Spitzer observations.

distribution, and predicts that the line will have a Gaussian shape. Equation 4 can then be numerically minimised to determine the optical depth, by assuming that  $\sigma = 0.64$ , which corresponds to the average full width half maximum (fwhm)  $v_{\text{fwhm}}$  of  $1.5$   $\text{km s}^{-1}$  that we measure across the cloud. The

abundance ratio was assumed to be the accepted value of  $X(^{13}\text{CO})/X(\text{C}^{18}\text{O}) = 8$  (Frerking et al. 1982). Only spectra with a peak line detection of  $> 3\sigma_{\text{rms}}$  were used for the  $^{13}\text{CO}$  and  $\text{C}^{18}\text{O}$  maps used to create the ratio map.

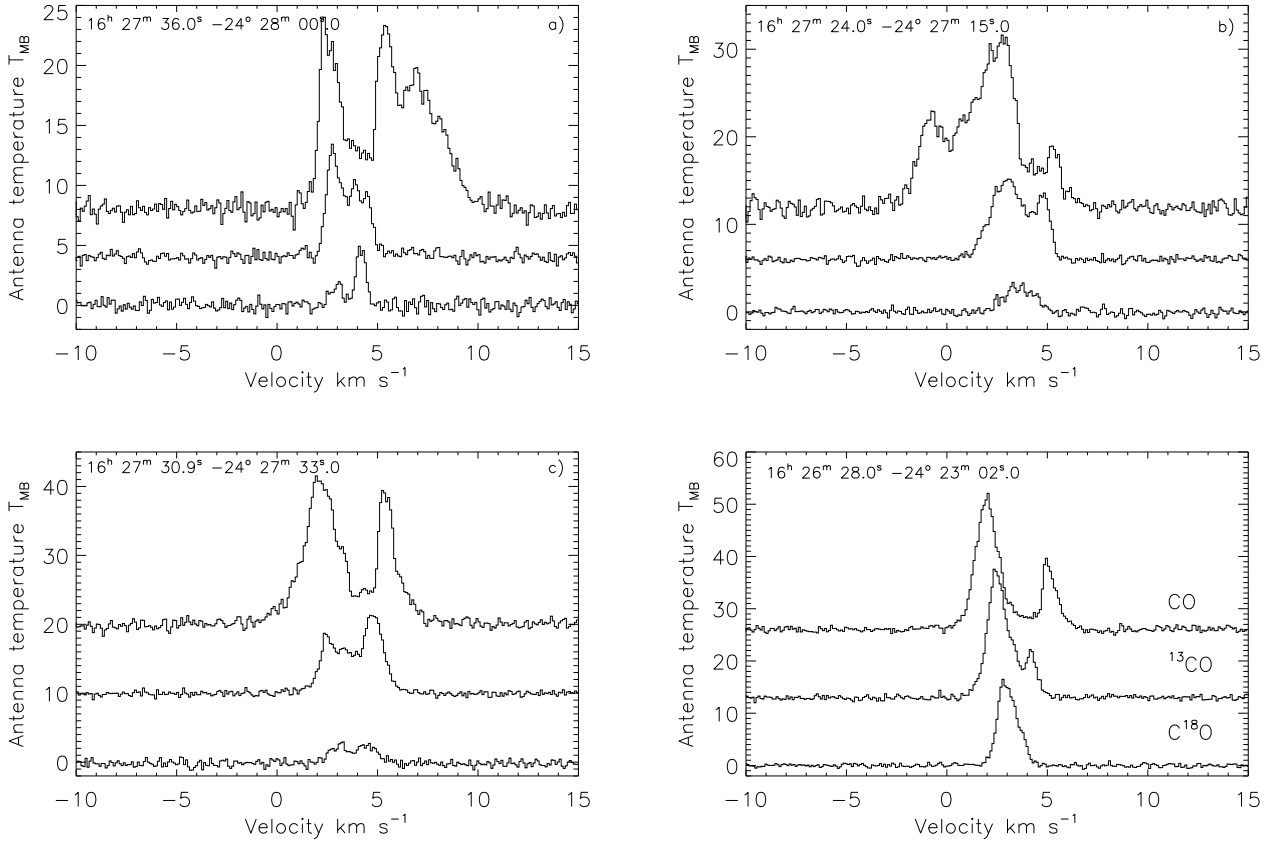


**Figure 6.** Typical spectra showing the data quality at two locations (each panel shows the CO,  $^{13}\text{CO}$  and  $\text{C}^{18}\text{O}$  lines ordered from top to bottom, as labelled in panel d). Panels a)–c) show the red and blue wings of an outflow in Oph B (see Section 5.2): a) Red wing RA(J2000) =  $16^{\text{h}}27^{\text{m}}36.0^{\text{s}}$ , Dec(J2000) =  $-24^{\circ}28'00.0''$ , b) Blue wing RA(J2000) =  $16^{\text{h}}27^{\text{m}}24.0^{\text{s}}$ , Dec(J2000) =  $-24^{\circ}27'15.0''$ , c) Central spectrum RA(J2000) =  $16^{\text{h}}27^{\text{m}}30.9^{\text{s}}$ , Dec(J2000) =  $-24^{\circ}27'33.0''$ . The second position in the cloud (d) shows spectra at the peak of the  $\text{C}^{18}\text{O}$  emission in the Oph A clump, where self absorption is very prominent at RA(J2000) =  $16^{\text{h}}26^{\text{m}}28.0^{\text{s}}$ , Dec(J2000) =  $-24^{\circ}23'02.0''$ .

Figure 8 shows the map of  $\tau(\text{C}^{18}\text{O})$ , where  $\tau(^{13}\text{CO})$  would be greater by the abundance factor of 8.

In Oph A, the typical integrated intensity ratios  $^{13}\text{CO}/\text{C}^{18}\text{O}$  are observed to range from  $\sim 2$ – $7$ , corresponding to  $\tau(^{13}\text{CO})$  of  $2 \rightarrow 16$  and  $\tau(\text{C}^{18}\text{O})$  of  $\sim 0.3 \rightarrow 2.0$ .  $^{13}\text{CO}$  is usually found to be optically thick around the main clumps, often also showing self-absorbed profiles.  $\text{C}^{18}\text{O}$  is also optically thick in some of the clumps, and toward the PDR. In particular  $^{13}\text{CO}$  emission from the PDR region is self-absorbed with a  $^{13}\text{CO}/\text{C}^{18}\text{O}$  integrated intensity ratio as low as 1.2 (where  $\tau(\text{C}^{18}\text{O}) > 5$ ).

Although the optical depth of  $\text{C}^{18}\text{O}$  throughout most of Ophiuchus is found to be optically thin ( $\tau < 1$ ), it is optically thick in some regions, indicating that an optical depth correction does need to be applied when calculating the mass from the integrated  $\text{C}^{18}\text{O}$  emission. Including all pixels with a peak  $T_{\text{MB}}$  of at least  $3\sigma_{\text{rms}}$  (1.36 K), the excitation temperature,  $T_{\text{ex}}$ , was calculated using the  $^{13}\text{CO}$  peak temperature (Section 4.1). In regions where  $T_{\text{ex}}$  was degenerate, or could not be uniquely estimated, the nominal excitation temperature of  $^{13}\text{CO}$  was assumed to be 20 K. The value of the abundance ratio of  $\text{C}^{18}\text{O}$  to  $\text{H}_2$ ,  $X_{\text{CO}}$  was assumed to be  $10^{-7}$  (Curtis et al. 2010, Graves et al. 2010), which is simi-

lar to the commonly used value from Frerking et al. (1982) of  $1.7 \times 10^{-7}$ . It should be cautioned that uncertainty remains concerning the question of whether CO abundances remain constant in molecular clouds, with recent work showing that  $X_{\text{CO}}$  may vary according to the local ISM environment, and that even within individual clouds can vary by factors of 3–4 (Lee et al. 2014).

The mass of the cloud mapped in the present observations is estimated to be  $515 M_{\odot}$  (or without the optical depth correction  $439 M_{\odot}$ ). Previous studies of star forming regions (Graves et al. 2010, Curtis et al. 2010, Buckle et al. 2010) have assumed a constant excitation temperature of around 10–12 K based on  $^{13}\text{CO}$  average excitation temperatures. Had the lower, constant excitation temperature been adopted, the mass would have been greater by a factor of  $\sim 1.6$ – $2.3$ .

### 4.3 Energetics of the Ophiuchus cloud

The virial mass of the region,  $M_{\text{vir}}$ , were calculated under the assumption that each of the clumps in the map are spherical and virialised with a density profile of the form  $\rho \propto r^{\beta}$ , where  $\beta$  is the density gradient. It is further assumed that

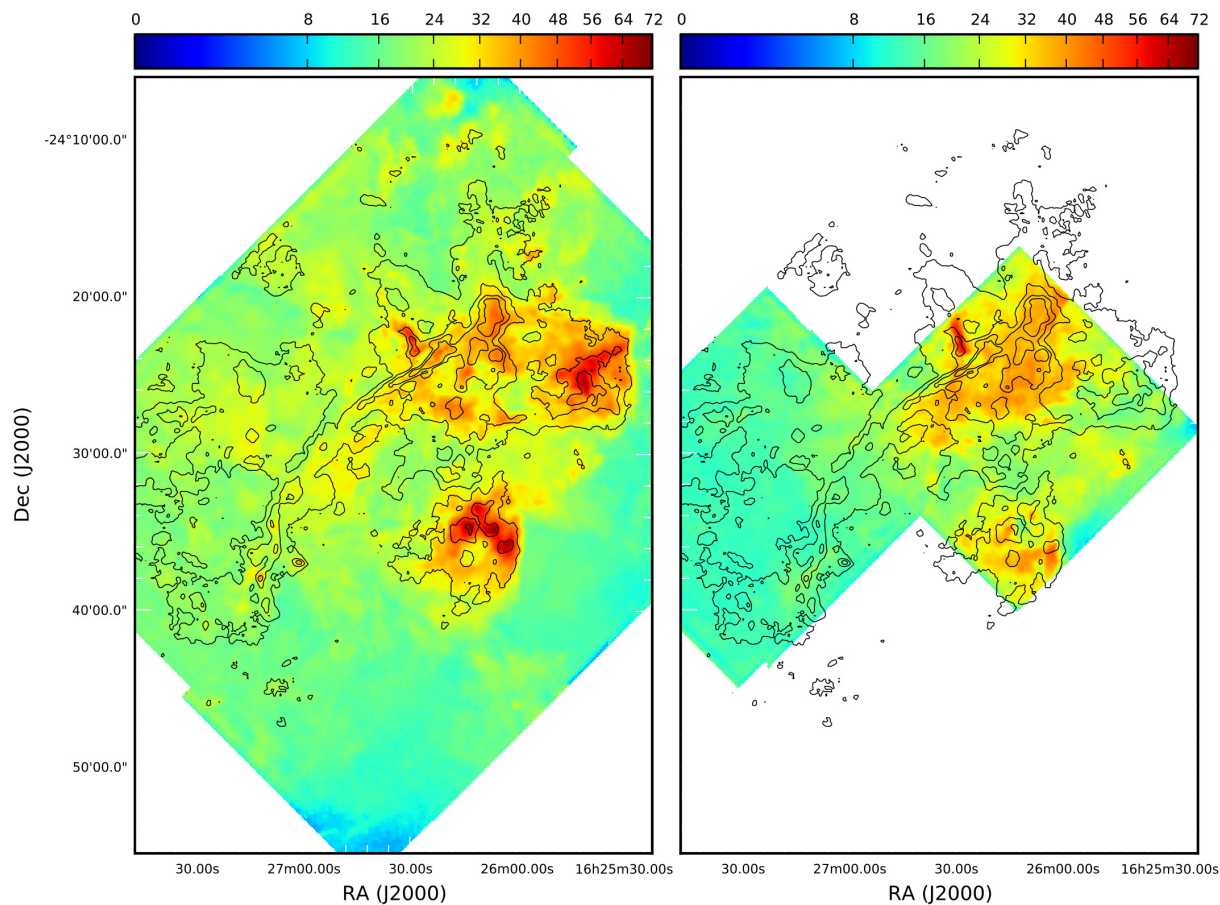


**Figure 7.** Excitation temperature maps (K) of  $T_{\text{ex}}(\text{CO})$  (left) and  $T_{\text{ex}}(^{13}\text{CO})$  (right) with contours from the CO integrated main-beam intensity at levels 50, 75, 100, and 125  $\text{K km s}^{-1}$ .

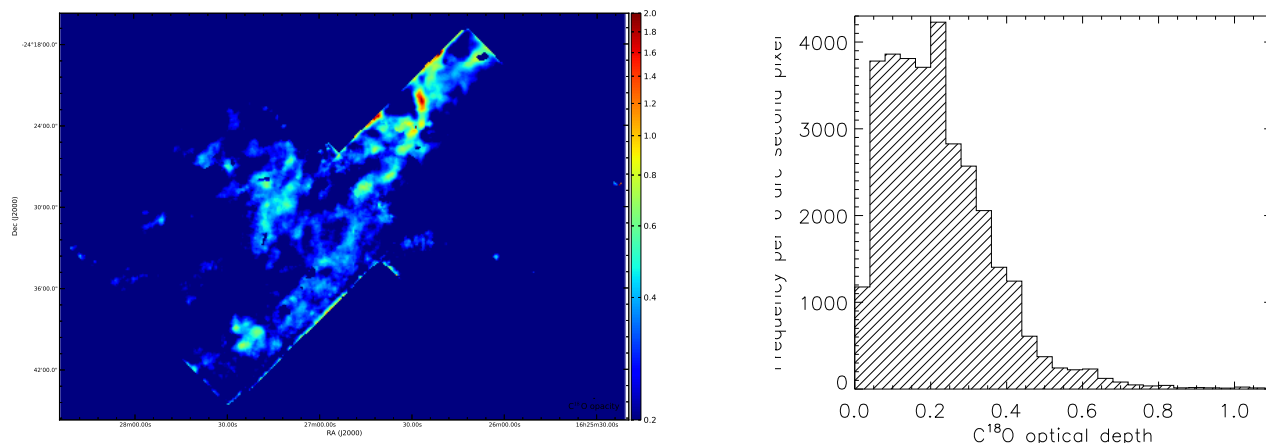


**Figure 8.** [Left] Map of the  $\text{C}^{18}\text{O}$  optical depth,  $\tau(\text{C}^{18}\text{O})$ , following the technique described in Equations 2 and 3 of Graves et al. (2010), reaching a maximum value of  $\sim 2$  in the Oph A clump region. [Right] Cumulative histogram plot showing the  $\text{C}^{18}\text{O}$  optical depth from the map on the left. The peak  $\text{C}^{18}\text{O}$  optical depth is  $\sim 0.2$ , with 96 per cent of the cloud area having an optical depth  $< 0.5$ .

there is no magnetic support or pressure confinement, and that the size of the Ophiuchus cloud is completely enclosed by the observations. Whereas it is clear that the large-scale structure of the Ophiuchus cloud is not strictly spherical, the assumptions above serve as a first order approximation of the geometry. Subject to these uncertainties, we have used the following relationship:

$$M_{\text{vir}} = \frac{5 \sigma^2 R}{\gamma G} \quad (5)$$

where we assume that  $\sigma$  is the 1D velocity dispersion  $\Delta v(\text{C}^{18}\text{O})/\sqrt{8 \ln 2}$ ,  $R$  is the radius of the cloud in parsecs,  $G$  is the gravitational constant and  $\gamma$  is given by:

$$\gamma = -\frac{1 + \beta/3}{1 + 2\beta/5} \quad (6)$$

which assumes that the density distributions of the clouds are spherical and follow an inverse square law. Here  $\gamma$  takes the value 5/3, following that used for the Serpens (Graves et al 2010) and Orion B studies (Buckle et al 2010).

The gravitational binding energy,  $E_{\text{grav}}$ , and the turbulent kinetic energy,  $E_{\text{kin}}$  can also be estimated using the relations:

$$E_{\text{grav}} = -\frac{3}{5}\gamma \frac{GM^2}{R} \quad \text{and} \quad E_{\text{kin}} = \frac{3}{2}M\sigma^2 \quad (7)$$

where  $G$  is the gravitational constant,  $M$  and  $R$  are the mass and radius (assumed spherical) of the cloud respectively, and  $\sigma = \Delta v_{\text{C}^{18}\text{O}}/\sqrt{8 \ln 2}$  represents the 1D velocity dispersion.

Throughout the Ophiuchus cloud, the average fwhm velocity  $\Delta v(\text{C}^{18}\text{O})$  was measured to be  $1.5 \text{ km s}^{-1}$  by fitting a Gaussian to the  $\text{C}^{18}\text{O}$  average spectrum across the cloud. The effective radius,  $R$  of the cloud was determined from  $A = \pi R^2$ , where  $A$  is the total pixel area of the map with peak  $T_{\text{MB}}$  detections of at least  $3\sigma_{\text{rms}}$ . This gave a radius of  $14'$  or  $0.5 \text{ pc}$  at  $120 \text{ pc}$  distance. Adopting these values, the virial mass is  $141 M_{\odot}$ .

The virial mass is therefore 27 per cent of the total estimated  $\text{C}^{18}\text{O}$  mass, indicating the Oph cloud as a whole is in a bound state, and most likely collapsing from an overall perspective. Our study agrees with results from past studies using  $^{13}\text{CO}$  1–0 (Loren et al. 1989; radius of  $0.3 \text{ pc}$  and  $1.5 \text{ km s}^{-1}$  velocity width) and  $\text{C}^{18}\text{O}$  1–0 (Tachihara et al. 2000; radius of  $0.4 \text{ pc}$  and  $1.5 \text{ km s}^{-1}$  velocity width) when corrected to a distance of  $120 \text{ pc}$ .

Loren et al. (1989a,b) estimated the virial mass was 24 per cent of the total gas mass ( $475 M_{\odot}$  gas mass and a virial mass of  $113 M_{\odot}$ ). Tachihara et al. (2000) found the virial mass to be 21 per cent of the cloud mass ( $455 M_{\odot}$  gas mass and a virial mass of  $97 M_{\odot}$  respectively). Similarly, Nakamura et al. (2011) calculated the virial mass to be 22 per cent of the mass for the total LDN1688 cloud (R21–22, R24–26) using the  $^{13}\text{CO}$  data from Loren et al. (1989a,b) where a distance of  $125 \text{ pc}$  and a radius of  $0.8 \text{ pc}$  was used. Our calculated virial mass is larger than these past studies due to the higher effective radius used in Equation 5.

## 5 MOLECULAR OUTFLOW IDENTIFICATION AND ANALYSIS

One of the objectives of this study was to investigate whether outflows in the Ophiuchus cloud are the main driving force of turbulence throughout the cloud. In this Section we first present the results from a search for molecular outflows across the mapped area, which will be followed by a discussion of the locations and interactions of these outflows with the more prominent clumps in the cloud.

Sections of the cloud close to thirty protostars selected from *Spitzer* data forming part of the survey ‘From Molecular Clouds to Planet-Forming Disks’ (c2d; Evans et al. 2009) were examined to search for evidence for molecular outflows. The c2d data was used by Padgett et al. (2008) to assign a spectral index  $\alpha_{2-24\mu\text{m}}$  to classify the sources following earlier work by Greene et al. (1994). We further extracted those sources with a spectral index  $\alpha_{2-24\mu\text{m}} > -0.3$ , which correspond to Class 0 and I sources and flat spectrum objects as listed in Table 2. Sources were also required to have a bolometric temperature (Myers & Ladd 1993)  $T_{\text{bol}} < 750 \text{ K}$  to further distinguish between more evolved flat spectrum sources bordering the Class II stage (where Class II protostars typically have a bolometric temperature range from  $650\text{--}2880 \text{ K}$  (Chen et al. 1995, 1997, André, Ward-Thompson & Barsony 2000)). The bolometric temperature cut-off was extended to  $750 \text{ K}$  in order to include flat spectrum sources IRS 45 and 47 previously studied for driving an outflow in the Oph B region (Kamazaki et al. 2001). The Class II source, WL 10, was also added due to past studies (Sekimoto et al. 1997) that have suggested it to be the driving source of its associated CO outflow.

Spectra from the locations of the 30 c2d protostars were examined on the CO  $J = 3\text{--}2$  map to search these sources for line wings that could be indicative of the presence of a molecular outflow. The method used followed the objective criterion introduced by Hatchell et al. (2007), which considers whether line-wings are detected in the CO spectra above  $T_{\text{mb}} = 1.5 \text{ K}$  at velocity separations of  $\pm 3 \text{ km s}^{-1}$  from  $v_{\text{LSR}}$ , the ambient cloud velocity. The systemic velocities of ambient material were estimated by fitting a Gaussian to the  $\text{C}^{18}\text{O}$   $J = 3\text{--}2$  spectra at the source coordinates.

$\text{C}^{18}\text{O}$  velocities calculated from the Gaussian fits at the positions of the protostars can be found in Table 2. The  $1.5 \text{ K}$  temperature criterion corresponds to  $T_{\text{mb}}$  rms values of  $\sim 5\sigma$  (depending on the source location in the map, after re-binning to a velocity resolution of  $1 \text{ km s}^{-1}$ ). Figure 14 shows the individual CO spectra re-binned to  $1 \text{ km s}^{-1}$  with the  $\text{C}^{18}\text{O}$  velocities and outflow criteria marked.

The results of the outflow analysis are summarised in Table 2, with the detection of either a blue and/or a redshifted line-wing noted for each source. The line wing criterion identifies not only those protostars driving molecular outflows, but also sources which are confused by emission from nearby outflows, or which have multiple velocity components along the line of sight. Outflow candidates identified as having a blue and/or a redshifted line-wing were further examined to determine whether the high-velocity emission detected is an outflow, and which source is the most likely driving source. Sources with potential confusion are labelled ‘y?c’ and the source number that could potentially cause confusion.

To summarise the result of the outflow survey: outflows were detected toward twenty-eight out of thirty sources (eight firm associations, with twenty being more marginal - primarily due to confusion with other potential driving sources within the beam). All of the protostars with firm outflow identifications have been previously reported in other studies (VLA 1623 AB, WL 10, Elias 29, WL 6, IRS 43, IRS 44 and IRS 54). Additionally the driver of the main Oph B outflow (IRS 47) is discussed separately in Section 5.2. Several new sources identified by the c2d survey have also been examined for the presence of a molecular outflow, these are labelled ‘SSTc2d’ in Table 2. The majority of these latter sources have some evidence for red and/or blueshifted outflow lobes, but again may be confused by other nearby protostars in this crowded region. Non-detections are found from 2 flat spectrum sources in Oph B and F regions. Flat spectrum objects are less embedded than Class 0/I sources and are more likely to not have outflow detections. Each of the main regions in Ophiuchus is discussed in more detail in Sections 5.1–5.4.

### 5.1 Oph A

The Ophiuchus cloud has been estimated to have a mass  $\sim 550 M_{\odot}$ , with the denser material distributed across 14 smaller clumps with diameters from 0.05–0.3 pc (Motte, André & Neri 1998) with masses from  $\sim 1$ –44  $M_{\odot}$ , which together have a total mass  $\sim 200 M_{\odot}$ . These authors identified 59 submm sources associated with starless cores, with diameters between  $\sim 1000$ –17,000 AU, and masses in the range 0.1–1.5  $M_{\odot}$ .

Oph A contains two Class 0, five Class I, and three flat spectrum protostars, dominated by VLA 1623 AB, and with potential outflows from SSTc2d J162614.6-242508, CRBR 2315, GSS 30, LFAM 1, GY 30, VLA 1623 W, SSTc2dJ1626.0-242340 and GY 91 with at least one high velocity outflow lobe. Figure 9 shows the H<sub>2</sub> 2.122  $\mu\text{m}$   $v = 1$ –0  $S(1)$  ro-vibrational line image of the Oph A region with contours of the red and blueshifted CO outflows overlaid.

The highly collimated outflow from VLA 1623 can be clearly seen in Figure 9. The prominent blueshifted lobe tracing the outflow extends roughly 0.7 pc across Oph A. VLA 1623 is composed of three sources (Murillo & Lai 2013, Ward-Thompson et al. 2011): VLA 1623 A (Class 0), VLA 1623 B (suggested to be either between prestellar and Class 0 stages, or a shocked knot in the jet) and VLA 1623 W (Class I), and is reminiscent of the multiple component protostellar system in the Lynds dark cloud LDN 723 (Avery, Hayashi & White 1990). We refer to VLA 1623 A and B as one source because it is unresolved in the c2d survey. Previous work (Murillo & Lai 2013, Dent & Clarke 2005) suggests that two distinct outflows make up the highly collimated Oph A outflow, potentially driven by VLA 1623 A and W. Due to confusion in the region, VLA 1623 AB is listed as the driver of this outflow, although in reality the situation appears to be much more complex, with recent 690 GHz submillimetre observations with ALMA revealing that the source IRAS 16293 B is also driving a south-east compact outflow (Loinard et al. 2013). The less prominent redshifted lobe from VLA 1623 to the north-west causes confusion in this region for Class I sources GY 30, GSS 30, LFAM 1, CRBR 2315, VLA 1623W

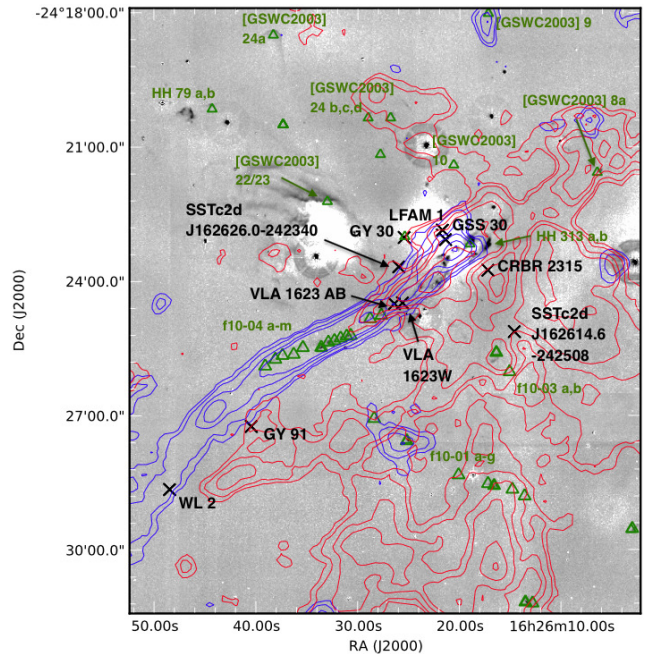


**Figure 9.** CO  $J = 3$ –2 outflows in Oph A, superimposed onto the UKIRT continuum-subtracted H<sub>2</sub> image. Blue contours are integrated from  $-8.6$ – $0.4$  km s<sup>−1</sup> and red contours are integrated from  $6.4$ – $15.4$  km s<sup>−1</sup>.

and Class 0 source SSTc2d J162626.0-242508. Each of these sources have both blue and red line-wing detections (SSTc2d J162626.0-242508 has a detection only in the red line-wing) using the CO outflow criterion. There is a possibility that H<sub>2</sub> knots in this region could be driven by outflows from these sources. GSS 30 and LFAM 1 have previously been noted as potential drivers for HH 313 b (Caratti o Garatti et al. 2006), [GSWC2003] 22a and 23c (Gómez et al. 2003), [GSWC2003] 9 and 10 (Gómez et al. 2003), [GSWC2003] 24b, 24c, and 24d (Gómez et al. 2003).

Similarly, high velocity gas was also seen towards GY 91 and WL 2, although whether these particular objects are the driving force of an outflow is not clear. These sources are located in the south of Oph A near the collimated blueshifted lobe of the VLA 1623 outflow. Each of these sources only has one high velocity component identified in the CO molecular outflow analysis, and neither source appears to show a bipolar outflow morphology in Figure 9. The blueshifted line-wing for WL 2 is most likely the result of the VLA 1623 outflow and the redshifted line-wing for GY 91 may be caused by other velocity components (i.e. by stellar winds from the nearby B2V stars). In addition to these sources, some high velocity blueshifted emission can be seen in this region directly corresponding to H<sub>2</sub> knots f10-01 a–g Khanzadayan et al. (2004), expected to be driven by Class II source YLW 31 (Bontemps et al. 2001).

### 5.2 Oph B

The Oph B region contains two distinct active centres, Oph B1 and Oph B2. These are separated by  $\sim 5$  arc minutes, and clearly shown in each of the isotopomeric lines shown in Figure 10, which shows a grey-scale plot of the region to

Source	Right Ascension (J2000)	Declination (J2000)	Name <sup>a</sup>	Class <sup>b</sup>	$v_{\text{LSR}}$ km s <sup>-1</sup>	Red Lobe	Blue Lobe	Verdict
1	16:26:14.63	-24:25:07.5	SSTc2d J162614.6-242508	0	2.8	y	n	y?c8
2	16:26:17.23	-24:23:45.1	CRBR 2315	I	3.1	y	y	y?c8
3	16:26:21.40	-24:23:04.1	GSS 30-IRS1, Elias 21	I	3.3	y	y	y?c8
4	16:26:21.70	-24:22:51.4	GSS 30-IRS3, LFAM 1	I	3.3	y	y	y?c8
5	16:26:25.46	-24:23:01.3	GY 30	I	3.3	y	y	y?c8
6	16:26:25.62	-24:24:28.9	VLA 1623W <sup>c</sup>	I	3.1	y	y	y?c8
7	16:26:25.99	-24:23:40.5	SSTc2d J162626.0-242340	flat	3.2	y	y	y?c8
8	16:26:26.42	-24:24:30.0	VLA 1623(AB)	0	3.4	y	y	y
9	16:26:40.46	-24:27:14.3	GY 91	flat	3.0	y	n	y?PDR
10	16:26:44.19	-24:34:48.4	WL 12	I	4.0	y	n	y?
11	16:26:48.47	-24:28:38.7	WL 2, GY 128	flat	3.2	n	y	y?c4
12	16:26:59.10	-24:35:03.3	SSTc2d J162659.1-243503	I	3.8	y	n	y?
13	16:27:02.32	-24:37:27.2	WL 16, GY 182	I	4.1	n	y	y?
14	16:27:05.24	-24:36:29.6	LFAM 26, GY 197	I	4.3	y	y	y?c17
15	16:27:06.75	-24:38:14.8	WL 17, GY 205	I	4.3	n	y	y?c17
16	16:27:09.09	-24:34:08.3	WL 10	II	3.4	y	y	y
17	16:27:09.40	-24:37:18.6	Elias 29, GY 214	I	4.3	y	y	y
18	16:27:16.39	-24:31:14.5	SSTc2d J162716.4-243114	flat	3.5	n	n	n
19	16:27:17.58	-24:28:56.2	IRS 3, GY 2447	I	4.1	n	y	y?c27
20	16:27:21.45	-24:41:43.0	IRS 42, GY 252	flat	3.8	y	n	y?
21	16:27:21.79	-24:29:53.1	WL 6	I	3.8	y	y	y
22	16:27:21.82	-24:27:27.6	SSTc2d J162721.8-242728	flat	3.7	n	y	y?c27
23	16:27:24.58	-24:41:03.1	CRBR 2422	I	4.0	y	n	y?24
24	16:27:26.91	-24:40:50.7	IRS 43, GY 265	I	3.7	y	y	y
25	16:27:27.99	-24:39:33.4	IRS 44, GY 269	I	3.8	n	y	y
26	16:27:28.44	-24:27:21.0	IRS 45, Elias 32	flat <sup>d</sup>	3.5	n	y	y?c27
27	16:27:30.17	-24:27:43.7	IRS 47, IRS 47	flat	4.0	n	y	y
28	16:27:30.91	-24:27:33.2	SSTc2d J162730.9-242733	I	3.8	y	y	y?c27
29	16:27:37.23	-24:42:37.9	GY 301	flat	3.7	n	n	n
30	16:27:51.79	-24:31:45.4	IRS 54, GY 378, YLW 52	flat	4.0	y	y	y

<sup>a</sup> VLA: André et al. (1990), GY: Greene & Young (1992), GSS: Gradalen et al. (1973), IRS: Allen (1972), Elias: Elias (1978), CRBR: Cameron et al. (1993), WL: Wilking & Lada (1983), Leous et al. (1991), SSTc2d: Evans et al. (2009).

<sup>b</sup> Classifications follow Greene et al. (1994), which is used in Padgett et al. (2008).

<sup>c</sup> Enoch et al. (2009) denote this source as VLA 1623.

<sup>d</sup> IRS 45 was listed as a Class II protostar by Wilking et al. (2001). However its spectral index (Greene et al. 1994) suggests that it may instead be a flat spectrum source, although its bolometric luminosity lies close to the boundary between Class I and II protostars.

**Table 2.** Outflow status for sources in Ophiuchus based on the criteria of outflow identification, discussed in Section 5.

the south-east that contains the Oph B clumps, along with clumps C, E and F. This shows the importance of mapping complex regions like this in a number of isotopologues as well as in the submm continuum, because of the effects of opacity on changing the apparent structures. For example, many of the small submm clumps seen in the 850  $\mu\text{m}$  image between Oph C, E, and F are also recovered in  $^{13}\text{CO}$  and  $\text{C}^{18}\text{O}$ , but may not be identified from the CO observations alone.

Oph B2 is the second densest region of LDN1688, and contains a number of 1.3 mm continuum sources that do not have infrared counterparts, and which are protostellar candidates (Motte, André & Neri 1998, Friesen et al. 2009). The Oph B2 clump appears to be rather colder than Oph A, with temperatures ranging from  $\sim 7\text{--}23$  K at the centre of the clump (Stamatellos et al. 2007), and with an outflow which has previously been believed to be powered by, or associated with the Class II object IRS-45 (also known as VSSG 18 or Elias 32), or IRS-47 (van der Marel et al. 2013).

The Oph-B region contains at least three Class I and five flat spectrum protostars. Three sources (WL 6, IRS 54,

and IRS 47) were confirmed to drive outflows with four additional sources being marginal molecular outflow candidates.

Figure 11 shows the  $\text{H}_2$  map with the outflows for this region overlaid as contours. The blue contours trace the blueshifted integrated CO intensity  $\int T_{\text{MB}} dv$  (from  $-6.0 \rightarrow 1.0$  km s<sup>-1</sup>) and the red contours trace the redshifted CO) integrated intensity (from  $7.0 \rightarrow 14.0$  km s<sup>-1</sup>). For both the contours are at 3, 5, 10, 15, 30, and 45 K km s<sup>-1</sup>.

Protostars SSTc2d J162730.9-242733, IRS 45, and IRS 47 can be seen in the central region of a large, clumpy outflow in Oph B (Figure 11). Kamazaki et al. (2001) attributed this outflow to IRS 45 due to its proximity to the strongest blueshifted emission in the lobe. The position-velocity diagram in Figure 12 clearly shows the redshifted lobe extending from the centre of IRS 47 and  $\sim 0.3'$  from IRS 45, also seen in Figure 11. We therefore suggest that IRS 47 is the driving source for this region due to its more central location between the blue and redshifted lobes, in agreement with the suggestion by van der Marel et al. (2013).

The bipolar outflow driven by Class I source WL 6 is

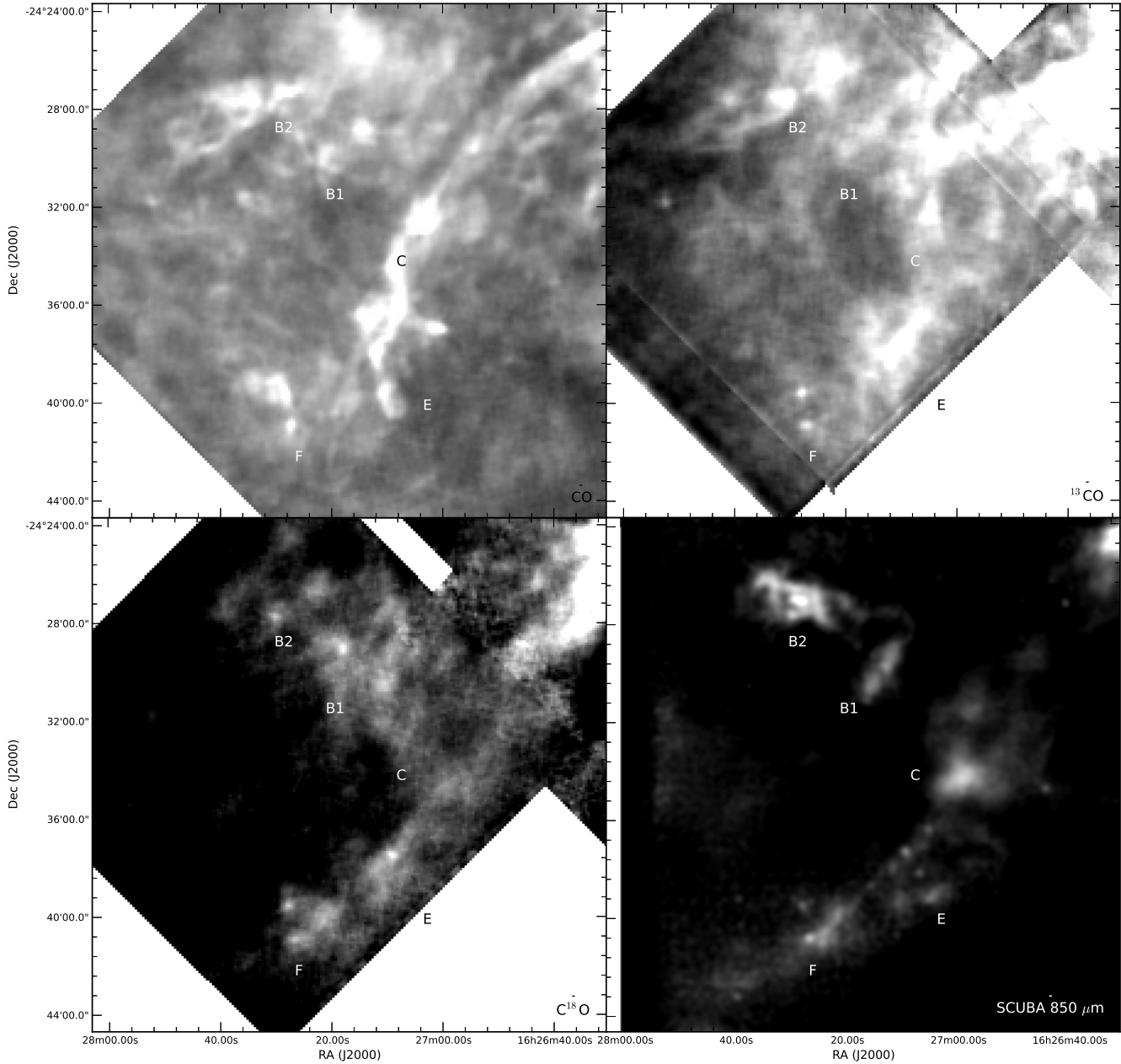


**Figure 10.** Greyscale plot of the Oph B, C, E and F clumps, where the three isotopologues are shown side by side, and on the same scale, to compare and contrast the appearance in the four isotopomeric lines. They figures are displayed in black and white to emphasise the changing structures between the isotopologue maps, and cosmetically saturated to emphasise the small scale structure in the data. To allow comparison the labels on the plots hold the same positions from line to line to set points of reference to guide the eye. Because of the non-linear transfer function used to enhance the features, some residual striping and joins between overlapping data blocks remain visible in the  $^{13}\text{CO}$  data at the few percent level, although this is at a very low level.

located south-west of IRS 47. Khanzadayan et al. (2004) has suggested that this source may drive the  $\text{H}_2$  knot f09-02 from the blueshifted lobe of the outflow. This outflow detection agrees with the observations of Sekimoto et al. (1997). The last firm bipolar outflow detection is from IRS 54 in the east of Oph B. IRS 54 is a binary with a  $7''$  separation based on near-IR observations (Haisch et al. 2006, Duchêne et al. 2004), which has been suggested by Jørgensen et al. (2009) to drive a bipolar precessing outflow. This source is also associated with  $\text{H}_2$  knots [G01] C1–5 (Grosso

et al. 2001) and f08-01 a–h (Khanzadayan et al. 2004, Gómez et al. 2003). In Figure 11, the location of the  $\text{H}_2$  knots and the high-velocity molecular gas associated with the outflow trace a curved path, further supporting the presence of a precessing outflow, similar to that reported in L1551 by Fridlund et al. 1989, 2002, 2005) and White et al. (2006).

Sources IRS 37 and SSTc2d J162721.8-242728 also have marginal molecular outflow detections with the blueshifted high velocity lobe present. These sources are located near the blueshifted lobe of the IRS 47 outflow, which is potentially

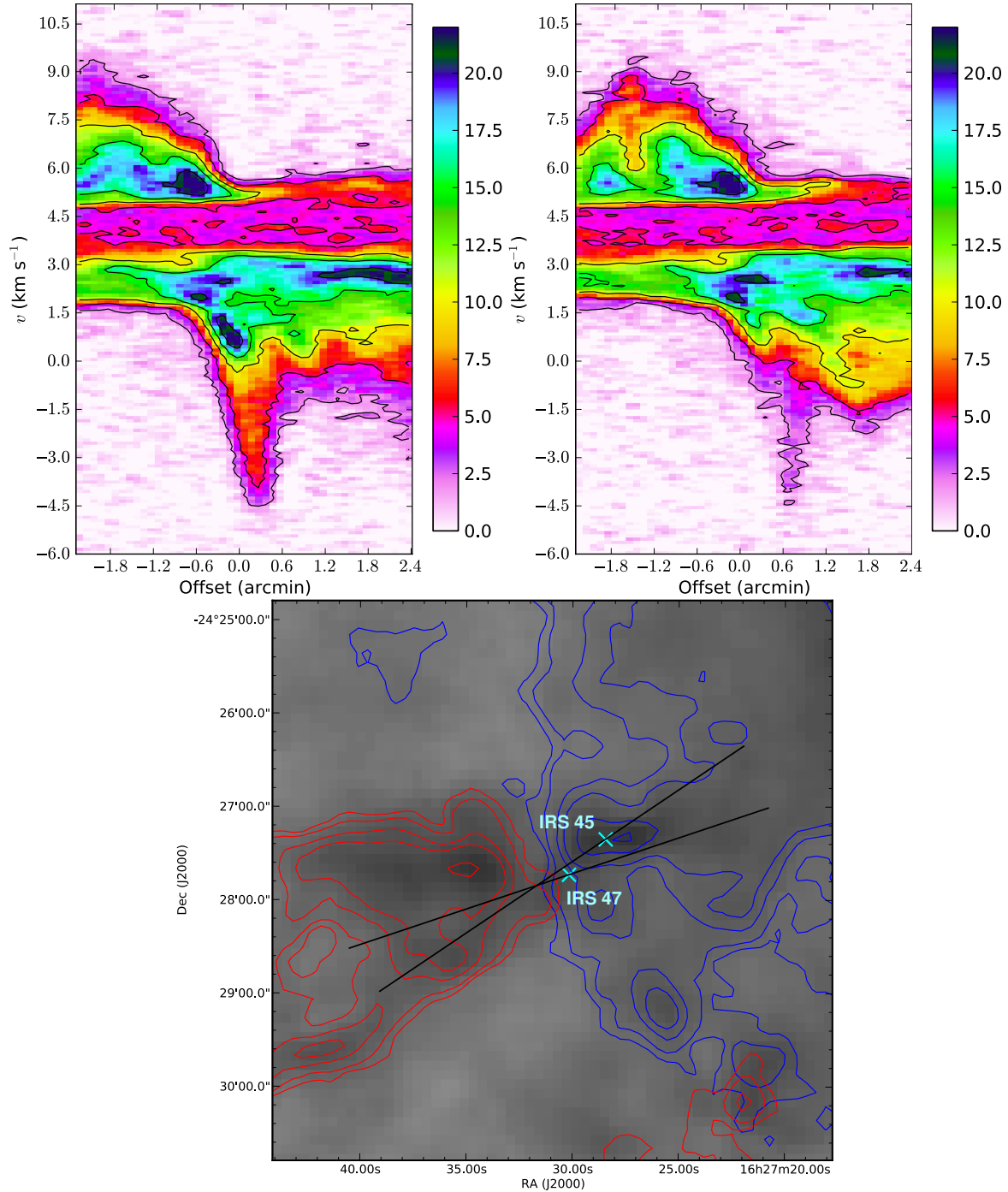


**Figure 12.** Position-velocity diagrams for sources IRS 45 (left) and IRS 47 (right). The cuts used for the position-velocity (PV) diagram are shown in the lower panel, along with the red and blue outflow lobes. The colour bar is shown in units of main beam brightness temperature  $T_{MB}$ .

the cause of the blue line-wing detection. No detection of an outflow was found for SSTc2d J162716.4-243114, a flat spectrum source south of the main Oph B outflow.

### 5.3 Oph C and E

The Oph C and E regions lie in the western/south-western of LDN1688. Although Oph-C lies within the area mapped by the CO observations, it is located just at the edge of the

$^{13}\text{CO}$  map, and just off edge of the  $\text{C}^{18}\text{O}$  map shown in Figure 10. Together, these regions contain six Class I protostars and one Class II protostar. Using the CO outflow criteria, two sources (Elias 29 and WL 10) are confirmed to drive outflows and five sources are identified as marginal molecular outflow candidates, with one having a high velocity line-wing detected. Figure 13 shows the  $\text{H}_2$  image with the blue and redshifted CO outflows for Oph C, E, and F superimposed as blue and red contours respectively.

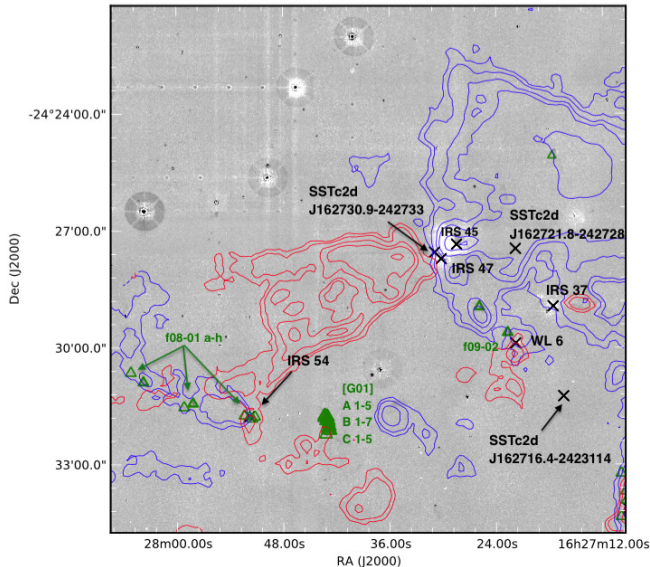


**Figure 11.** CO  $J = 3-2$  outflows in Oph B. Blue contours trace the blueshifted CO intensity  $\int T_{\text{MB}} dv$  (integrated from  $-6.0$  to  $1.0 \text{ km s}^{-1}$ ) and red contours trace the redshifted CO intensity (integrated between  $7.0$  and  $14.0 \text{ km s}^{-1}$ ); contours are at 3, 5, 10, 15, 30, and  $45 \text{ K km s}^{-1}$ .

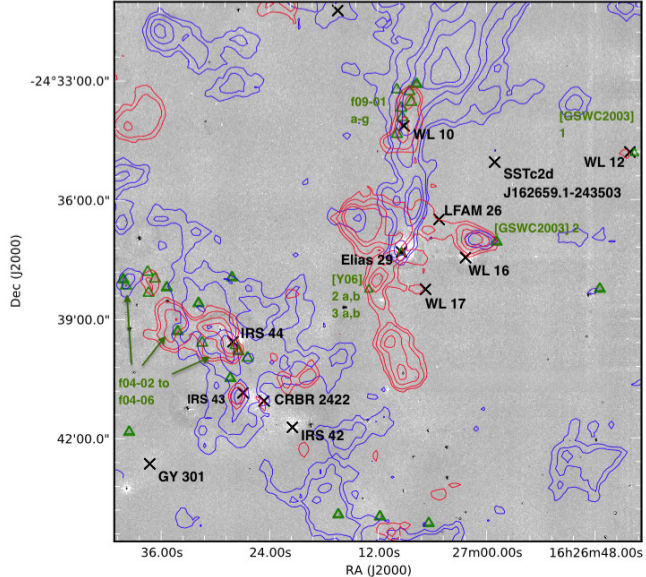


**Figure 13.** CO  $J = 3-2$  outflows in Oph C, E, and F. Blue contours trace the blueshifted CO intensity  $\int T_{\text{MB}} dv$  (integrated from  $-5.7$  to  $1.3 \text{ km s}^{-1}$ ) and red contours trace the redshifted CO intensity (integrated from  $7.0$  to  $14.3 \text{ km s}^{-1}$ ); contours are at 3, 5, 10, 15, 30, and  $45 \text{ K km s}^{-1}$ .

The bipolar outflow driven by Elias 29 can be clearly seen in Figure 13. This outflow is known for its s-shape (Bontemps et al. 1996, Sekimoto et al. 1997, Bussmann et al. 2007), which has been suggested to be a consequence of a precessing outflow associated with a binary system (Ybarra et al. 2006), similar to that of L1551 (White et al. 2006). The outflow encompasses several  $\text{H}_2$  knots, mainly in the southern redshifted lobe, which are labelled 2 a,b and 3 a,b

from Ybarra et al. 2006. Gómez et al. (2003) also suggest that the knot [GSWC2003]2 is driven by Elias 29, aligning with the east-west CO emission that appears to be driven by the source. The blueshifted outflow lobe extends to the north, also potentially driving several knots near the Class II protostar WL 10. WL 10 lies north of Elias 29 in the Oph C region and is known to be associated with a bipolar outflow (Sekimoto et al. 1997) that can also be seen in Figure 13. The outflow encompasses  $\text{H}_2$  knots f09-01 a–g (Khanzadayan et al. 2004). Gómez et al. (2003) and Zhang et al. (2011) have attributed f09-01 b,e–g to the outflow, although f09-01 a,c,d may also be related to the CO outflow from WL 10. The latter knots have been previously been attributed to WL 16 (Gómez et al. 2003, Zhang et al. 2011).

Sources LFAM 26, WL 17, and WL 16 lie near Elias 29 and could suffer confusion from the high-velocity emission from its outflow. LFAM 26 and WL 17 have both blue and redshifted line-wings, and LFAM 26 has been classified as a driving source for an outflow by previous studies (Bussmann et al. 2007, Nakamura et al. 2011). Neither of these sources have strong bipolar lobes in Figure 13 and both lie directly to the west of Elias 29. WL 16 has a faint detection of a blue line-wing and past studies (Gómez et al. 2003, Zhang et al. 2011) have suggested that the source drives  $\text{H}_2$  knots f09-01 a,c,d near WL 10. WL 12 is located in the western portion of Oph C and has only a slight redshifted line-wing Bontemps et al. (2006) classified this source as driving a molecular outflow but considered it a more uncertain detection because the source did not have a bipolar detection, which is reflected in our study. Lastly, Class I source SSTc2d J162659.1-243503 has a faint detection of a red line-wing.

## 5.4 Oph F

The Oph F region makes up the south-eastern portion of the LDN1688 cloud, and was covered in all three of the isotopologues shown in Figure 10. The region contains four Class I and one flat spectrum protostars, each of which was examined for the outflow study. Using the CO outflow criteria, two sources (IRS 43 and IRS 44) are confirmed to drive outflows, two sources are identified as molecular outflow candidates with one high velocity line-wing detected, and one source does not have a clearly discernible associated outflow. In Figure 13, the bipolar outflows driven by IRS 43 and IRS 44 can be clearly seen. These outflow sources have been confirmed by past studies (IRS 43: Bontemps & André 1997; IRS 44: Bontemps et al. 1996, Bussmann et al. 2007).  $\text{H}_2$  knots attributed to the two sources are labelled f04-02 to f04-06 (Khanzadayan et al. 2004). IRS 42 and CRBR 2422 are located south of IRS 44 and IRS 43.

There were marginal outflow detections from the sources CRBR 2422 and IRS 42, located to the south-west of IRS 43 and IRS 44. These sources only have a faint red line-wing detected. Due to their proximity to IRS 43 and IRS 44, the line-wing detection is most likely the result of confusion caused from the nearby outflows. Additionally, there was not an outflow detection from flat spectrum source GY 301.

### 5.5 Outflow mass and energetics

The CO  $J = 3-2$  gas at high blue and redshifted velocities relative to the systemic velocity,  $v_{LSR}$  (e.g. see Figure 14), was used to calculate the global outflow mass and energetics of the cloud. To exclude the contribution from ambient cloud emission, the central line velocity,  $v_0$ , was estimated by using the average  $C^{18}O$  spectrum of the cloud, which was then fitted with a Gaussian to determine the line centre, and found to be  $3.3 \text{ km s}^{-1}$ . The line criterion used to identify the presence of outflows was (following Hatchell et al. 2007) to select spectra where the linewidths were broader than that assumed to be associated with ambient gas, by searching for lines where  $T_{mb}$  at offsets of  $\pm 2.5 \text{ km s}^{-1}$  from  $v_0 > 1.5 \text{ K}$ .

The criterion used to estimate the global energetics is similar to the outflow criterion but it takes into account global effects including the changes of the line centre of up to  $1 \text{ km s}^{-1}$  seen across the cloud, so as to better estimate the velocity range counted as ambient over that of the outflow gas. However, some ambient emission will be included in these calculations because there is no fixed velocity boundary between outflow-driven gas, and that of gas set in motion by ambient cloud turbulence. CO spectra of sources listed in Table 2 are shown in Figure 14. Specifically the central source velocities were calculated by fitting a gaussian to each individual  $C^{18}O$  spectrum, which should trace the ambient cloud rather than the outflow gas.

#### 5.5.1 Line opacities in the outflow line wings

The CO and  $^{13}CO$   $T_{mb}$  ratio can be used to estimate the CO opacity per velocity channel,  $\tau_{12}(v)$ . The maps were averaged to a single spectrum and clipped at  $3\sigma_{rms}$  and  $1\sigma_{rms}$  for CO and  $^{13}CO$  respectively. This enhanced the velocity range ( $\sim 0-9 \text{ km s}^{-1}$ ) allowing  $^{13}CO$  to be detected in the line-wings for the opacity calculation. The CO optical depth was then estimated using the following relation (e.g. Hatchell et al. 1999b, Curtis et al. 2010, Graves et al. 2010):

$$\frac{T_{12}}{T_{13}} = \left(\frac{\nu_{12}}{\nu_{13}}\right)^2 f_{13} \left(\frac{1 - \exp(-\tau_{12})}{\tau_{12}}\right) \quad (8)$$

where  $T$  is the main-beam temperature of each CO transition,  $\nu$  is the frequency of the isotopologues,  $f_{13}$  is the relative abundance of CO to  $^{13}CO$  (77; Wilson & Rood 1994), and  $\tau_{12}$  is the optical depth of CO. This assumes that  $^{13}CO$  is optically thin and CO is optically thick (see Hatchell et al. 1999a, Curtis et al. 2010). In this case, the ratio of observed antenna temperatures,  $T(\text{CO})/T(^{13}\text{CO}) = (1 - \exp(-\tau_{12})) / (1 - \exp(-\tau_{13}))$ , where  $\tau_{12} = X \tau_{13}$ , where  $X$  is the abundance ratio between the two molecules. Then, if  $\tau_{13}$  is optically thin,  $1 - \exp(-\tau_{13}) = \tau_{13}$ . This approach accounts for the differences in frequency of occurrence between the two molecules, with the ratio between the temperature of the two molecules decreasing with increasing CO optical depth.

Even though CO is expected to be optically thin in the high velocity blue and redshifted line-wings,  $^{13}CO$  does not extend as far in velocity range as the CO emission. Therefore, this equation was solved by assuming  $\tau_{12} \rightarrow \infty$  so that  $1 - \exp(-\tau_{12}) \approx 1$ .

Figure 15 shows the variation of the ratio of CO to  $^{13}CO$  main-beam temperatures with the calculated CO op-

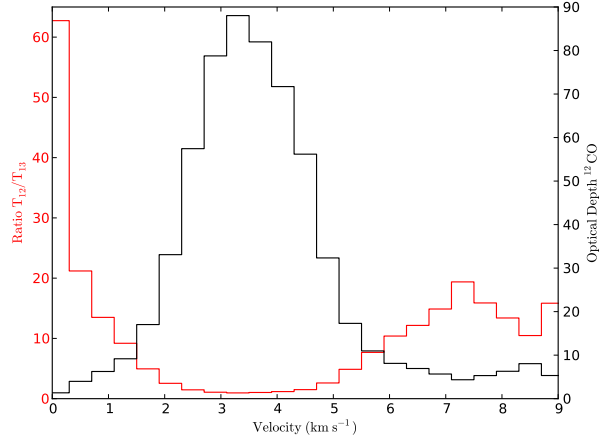


**Figure 15.** CO optical depth variation with velocity,  $\tau_{12}(v)$ . The ratio of CO to  $^{13}CO$  is shown as a function of velocity (red) and the CO optical depth is shown for the same velocity region (black).

tical depth per velocity channel. The CO emission is optically thick ( $\tau_{12} > 1$ ) over the velocity range  $0 \rightarrow 9 \text{ km s}^{-1}$ . The limit of the CO optical depth measurement is  $\tau_{12} \sim 3$ . The ratio of CO and  $^{13}CO$  main-beam temperatures supports the suggestion that CO is optically thick because the ratio only begins to approach the abundance ratio at the edges of the velocity range. We note the ratio at redshifted velocities ( $\sim 7-9 \text{ km s}^{-1}$ ) does not fully reach the abundance ratio, indicating that CO is still optically thick in this range. The opacity correction applied to the CO main-beam temperature is further discussed in Section 5.5.

Assuming local thermodynamic equilibrium, the outflow masses were calculated assuming a distance of 120 pc, with and without optical depth corrections per velocity channel, and an assumed excitation temperature of 50 K (Hatchell et al. 2007, Curtis et al. 2010, Graves et al. 2010). The column density of a diatomic molecule may be estimated using the emission from a line (such as the  $(J+1) \rightarrow J$  transition) of an optically thin (ner, than CO) isotopomer; for the example of the  $J = 3-2$  transition (following Richardson et al. 1985, Kamazaki et al. 2003), and assuming local thermodynamic equilibrium, the mass can be estimated as:

$$M_{CO} = 3.77 \times 10^{-8} \left(\frac{X_{CO}}{10^{-4}}\right)^{-1} \left(\frac{d}{120 \text{ pc}}\right)^2 \times \left(\frac{A_{\text{pixel}}}{\text{arcsec}^2}\right) \sum_j \left(\int T_{MB,j} dv\right) M_{\odot} \quad (9)$$

where  $X_{CO}$  is the relative abundance of CO to  $H_2$  (Blake et al. 1987),  $A_{\text{pixel}}$  is the pixel area ( $36 \text{ arcsec}^2$ ),  $d$  is the distance (in parsecs), and  $j$  is an index over map pixels.

To estimate the momentum and energy,  $\int T_{MB} dv$  is replaced by  $\int T_{MB}|v - v_0| dv$  and  $\frac{1}{2} \int T_{MB}(v - v_0)^2 dv$  respectively, where  $v_0$  is the line centre for the cloud. The correction for CO optical depth, the integrated-main beam intensity becomes

$$\int T_{\text{corr}} dv = \int T_{MB} \frac{\tau_{12}}{1 - \exp(-\tau_{12})} dv \quad (10)$$

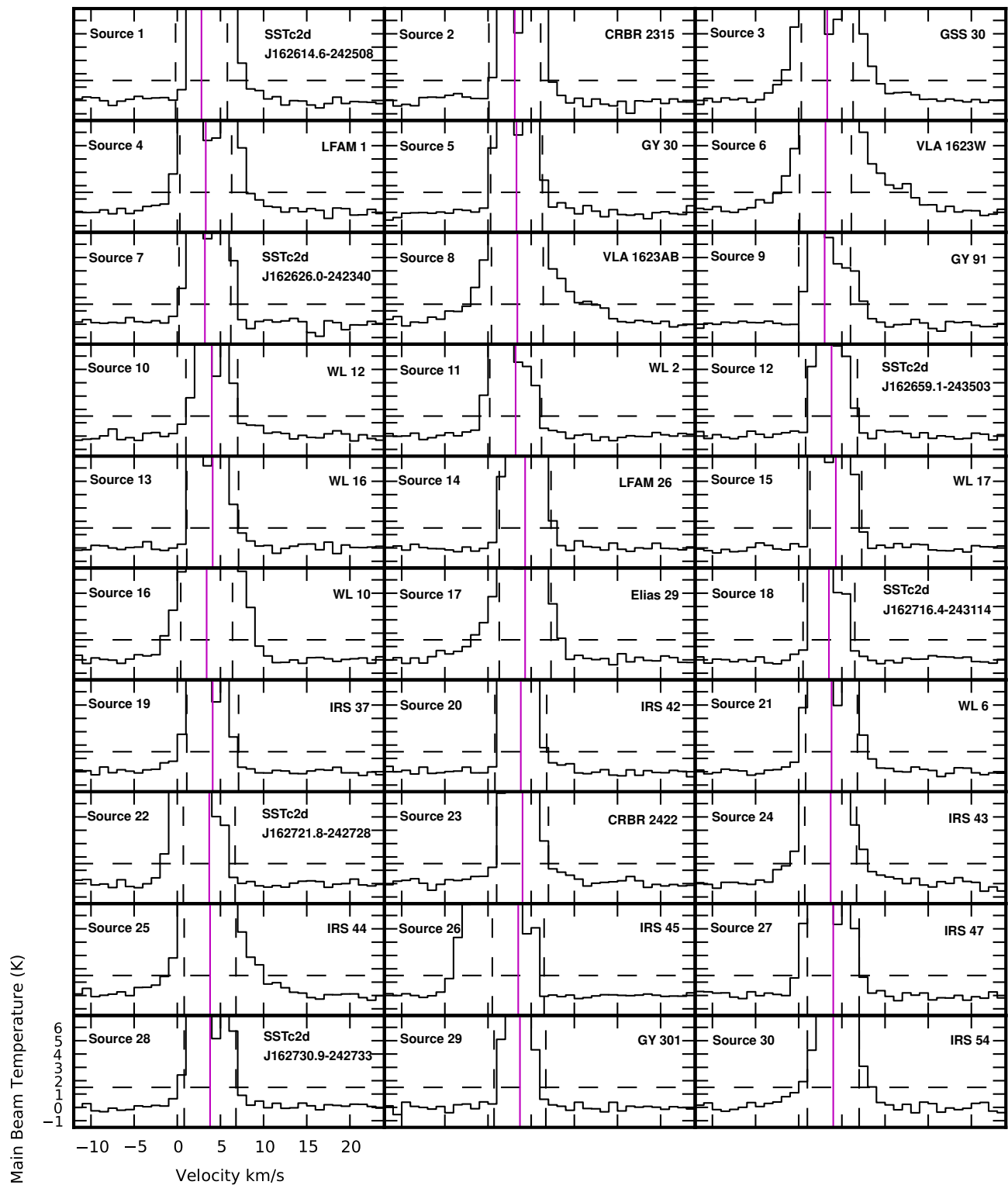


**Figure 14.** CO spectra of sources listed in Table 2, where the solid vertical line represents the systemic velocity (i.e.  $v_{LSR}$  of the line centroid of the  $C^{18}O$  line at the same position, the dashed vertical lines are drawn at  $\pm 3$  km s $^{-1}$  from this, and the dashed horizontal lines show the  $T_{mb} = 1.5$  K level).

	Mass ( $M_{\odot}$ )	Momentum ( $M_{\odot} \text{ km s}^{-1}$ )	Energy ( $M_{\odot} \text{ km}^2 \text{ s}^{-2}$ )
Thin			
Blue	0.20	0.74	1.49
Red	0.54	1.74	3.18
Corr.			
Blue	0.42	1.36	2.36
Red	4.30	12.67	19.85

**Table 3.** Global kinematics for the out-flowing gas assuming optically thin CO line-wing emission (thin) and with an optical depth correction (corr.).

and the momentum and energy estimates are corrected similarly. Blue- and redshifted main-beam temperatures are integrated from  $-8 \rightarrow 0.8$  and  $5.8 \rightarrow 15 \text{ km s}^{-1}$  respectively and the opacity correction is applied to the corresponding velocity channels between  $0 \rightarrow -9 \text{ km s}^{-1}$ . The velocity channel limits were based on whether or not there was detectable CO emission at the  $1\sigma_{\text{rms}}$  level.

The basic kinematics for the global out-flowing gas in Ophiuchus are summarised in Table 3. The mass, momentum, and energy increase substantially by factors of 6.4, 5.7, and 4.8 respectively when the optical depth of CO is taken into account. Effects involving outflow inclination angle can also greatly reduce the amount of momentum and energy observed. A correction for inclination can be applied to the blue and redshifted velocities for momentum and energy calculations. The line of sight velocities should be corrected by a factor of  $1/\cos(i)$ , where  $i$  is the inclination angle. Assuming random inclinations to the line of sight with uniformly distributed outflows ( $i \approx 57.3 \text{ deg}$ ; Bontemps et al. 1996), the momentum will increase further by a factor of 2 and the energy by a factor of 3 (Curtis et al. 2010). A detailed discussion of the efficacy of outflow properties as estimated from molecular line data is given by van der Marel et al. (2013), who show that the main techniques adopted in most studies agree to within a factor of  $\sim 6$ –10, differences of which can be reconciled by comparing the analysis methods.

The kinetic energy generated by the global high-velocity outflows can also be compared to the overall turbulent kinetic energy. When inclination and optical depth are taken into account, the total outflow kinetic energy is  $1.3 \times 10^{38} \text{ J}$  ( $67 M_{\odot} \text{ km}^2 \text{ s}^{-2}$ ) or 21% of the turbulent kinetic energy shown in Table 4. This suggests that outflows are significant but not the dominant source of turbulence in Ophiuchus. Conversely, Nakamura et al. (2011) suggested that protostellar outflows can drive turbulence in the region after finding the total outflow energy injection rate ( $L_{\text{tot}} \sim 0.2 L_{\odot}$ ) larger than the turbulent dissipation rate of the supersonic turbulence ( $L_{\text{turb}} \sim 0.06$ – $0.12 L_{\odot}$ ) assuming optically thin emission. A similar method was used to calculate the global outflow energy injection rate  $L_{\text{global}} = E_{\text{out}}/T_1$  where  $E_{\text{out}}$  is the global outflow kinetic energy and  $T_1$  is the lifetime of the Class I protostellar phase ( $\sim 0.5 \text{ Myr}$ ; Evans et al. 2009). This gives a global outflow energy injection rate  $L_{\text{global}} = 0.02 L_{\odot}$ , which is a factor of 10 smaller than the injection rate from Nakamura et al. (2011). The difference between the outflow energy injection rates is mainly due to our assumption that a longer outflow time-scale better re-

flects the age of Class I protostars, as opposed to calculating the dynamical time-scales of individual outflows.

Comparing our lower outflow injection rate to the turbulent dissipation rate from Nakamura et al. (2011) suggests that the global outflow injection rate is lower than the turbulent dissipation rate by a factor of 3–6. Additionally, optical depth corrections can be made to the turbulent dissipation rate which would further increase the difference between the injection and dissipation rates. This result agrees with our conclusion that global outflows in the Ophiuchus region are significant but not necessarily the dominant driver of turbulence in the cloud.

Supersonic turbulence would however dissipate rapidly, requiring that a power source other than outflows would have to be sustained for Ophiuchus. The energy needed might potentially come as a consequence of virialisation as clouds/clumps collapse, with turbulence generation occurring on a time scale of a few dynamical times ( $\sim 10^6 \text{ yr}$  for gas with a density  $\sim 10^4 \text{ cm}^{-3}$  from Hocuk & Spaans 2010).

The mass of the cloud estimated earlier in Section 4.2 using the  $\text{C}^{18}\text{O}$  integrated intensity, and the virial mass of the cloud assuming a spherical cloud of uniform density (Rohlfs & Wilson 2000) are both estimated and summarised in Table 4.

For Ophiuchus, the gravitational binding energy is estimated to be  $4.5 \times 10^{39} \text{ J}$  ( $2282 M_{\odot} \text{ km}^2 \text{ s}^{-2}$ ), and by using  $v_{\text{rwhm}}$  from the average  $\text{C}^{18}\text{O}$  linewidth across the cloud, the turbulent kinetic energy is estimated to be  $6.3 \times 10^{38} \text{ J}$  ( $320 M_{\odot} \text{ km}^2 \text{ s}^{-2}$ ). The turbulent kinetic energy is therefore roughly a factor of 7 smaller than the gravitational binding energy, suggesting that the cloud is gravitationally bound.

## 6 MOLECULAR CLUMP IDENTIFICATION AND ANALYSIS

The basic properties of the spatial distribution of the gas in the Ophiuchus complex were estimated using the *CPROPS* package (Rosolowsky & Leroy 2006) to identify clumplets, based on the  $\text{C}^{18}\text{O}$  maps (because this isotopomer is the least opaque of those studied). The properties of molecular clumplets were then estimated along with information from the other isotopomeric lines, that minimised the biases introduced by finite signal-to-noise and spatial resolution. The recovered data were then used (by assuming that all material was at the adopted distance to the Oph cloud) to estimate the molecular line luminosities and other properties such as their temperatures.

*CPROPS* initially searches for contiguous, significant emission ( $\geq 3\sigma$ ) compared to nearby emission free parts of the spectrum) in the  $\text{C}^{18}\text{O}$  position-velocity data cube, after decomposing the area surveyed into individual clumplets. Regions having areas less than that of two beam footprints are discarded, along with any detections where the emission was only detected in a single ( $0.1 \text{ km s}^{-1}$ ) velocity channel. To account for diffuse emission from the turbulent bulk of the cloud, the  $\text{C}^{18}\text{O}$  data were filtered using an *à trous* wavelet algorithm, similar to that described in Alves, Lombardi & Lada (2007). This algorithm removes large scale emission, whilst preserving small scale clump structures, without introducing significant negative features, which is a common limitation of Fourier filtering. This also helps to

Cloud	Total mass ( $M_{\odot}$ )	$E_{\text{kin}}^{\dagger}$ (J)	$E_{\text{grav}}^{\dagger}$ (J)	Outflow Energy (J)
Ophiuchus	515	$6.3 \times 10^{38}$	$4.5 \times 10^{39}$	$1.3 \times 10^{38}$

**Table 4.** Global mass and energetics.

avoid the confusion imparted by the background emission, which has in the past been another limiting factor in estimation of clump mass spectra when using algorithmic approaches. Specifically, we removed scales on the top three levels of a  $B_3$  cubic spline wavelet transform (see Starck & Murtagh 2006 for details), that corresponded to scales of 0.2 pc and larger. We then used the *CPROPS* algorithm to identify clumplets within the filtered cube, identify local maxima in the data, find shared surfaces, and to estimate the relative proportions of the emission attributable to each of the cloud clumplets. The algorithm identifies regions of position-position-velocity space associated with clumplets to calculate the properties of clumplets in the original  $\text{C}^{18}\text{O}$  data (pre-filtering), as well as of the corresponding regions in the  $^{13}\text{CO}$  and  $\text{CO}$  data sets. This joint analysis produces a matched catalogue of clumplets across all three isotopologue data cubes.

The default implementation of this is a watershed algorithm, similar to the widely used Clumpfind program, but which does not ‘fight’ over emission that is contested between objects. A first order correction for sensitivity bias was made using the methodology described by Rosolowsky & Leroy (2006) to extrapolate the measured parameters of the cloud structures to those expected for a cloud(s) with a boundary iso-surface of  $T_{\text{edge}} = 0$  K (i.e. assuming perfect sensitivity and an isolated single source, following the original formulation (Blitz & Thaddeus (1980), Scoville et al. 1987). Finally, the properties of the individual clumplets were measured, based on the extracted values from *CPROPS*. The performance of this clump extraction technique has been shown to compare favourably with other extraction codes such as *GAUSSCLUMPS* and *CLFIND* (see Rosolowsky & Leroy 2006, and Bolatto et al. 2008 for details). The robustness, reliability, and consistency of *CPROPS* appears to be very good for clouds having signal-to-noise ratios ( $s/n$ )  $> 10$ .

The clump properties were estimated using moments of the intensity distribution. The radii ( $R$ ) and velocity dispersions ( $\sigma_v$ ) were calculated from the intensity-weighted second moments in the spatial and velocity dimensions respectively, with the values of the radii reported in this paper being deconvolved from the gaussian telescope beamwidth. Clump masses were then characterised by a virial and a luminous mass estimate. The virial mass estimate is calculated adopting a  $\rho(r) \propto r^{-1}$  profile, following Scoville et al. (1987). Luminous masses were then estimated from the integrated  $\text{CO}$  flux  $S_{\text{CO}}$  using a constant  $\text{CO}$ -to- $\text{H}_2$  conversion factor:

$$M_{\text{lum}} = 0.011 S_{\text{CO}} \left[ \frac{X_{\text{CO}}}{2 \times 10^{20} \text{ cm}^{-2} (\text{K km s}^{-1})^{-1}} \right] D^2 M_{\odot} \quad (11)$$

where  $S_{\text{CO}} = \int I_{\text{CO}} d\Omega dv$  is the integrated  $\text{CO}$  flux in units of  $\text{Jy km s}^{-1}$ ,  $D$  is the distance to the source in kpc, and  $X_{\text{CO}}$  is the  $\text{CO}$ -to- $\text{H}_2$  conversion factor appropriate for  $\text{CO}(1-0)$  data, and includes a contribution to the mass from

He (see Bolatto et al. 2008 for further details). It should be noted that  $X_{\text{CO}}$  may vary for very high  $\text{CO}$   $J$ -transitions, if these are dominated by higher excitation material (see detailed discussion of this by Papadopoulos et al. 2012a,b), but at the moment there is no evidence to suggest a significant variation to this quantity between the  $\text{CO}$   $J = 1-0$  and  $3-2$  transitions. As a further cautionary note, that the Ophiuchus region suffers from widespread self-absorption by line of sight  $\text{CO}$ , and further we note that the  $\text{C}^{18}\text{O}$  line is optically thick at a few locations - both of these effects may in practice introduce some uncertainty to the luminous, and virial mass estimates (see Rosolowsky & Leroy 2008 for further details), although there is no reason to believe that these will provide a significant bias to the results.

The results of the clump decomposition are shown in Table 5, with the full catalogue of 105 clumplets being given in the supplementary material to this paper.

To estimate the completeness limit, experience with *CPROPS* suggests that, for the masking parameters used, the catalogue is complete for clumplets larger than 2 beam areas at the  $3\sigma$  level in the  $\text{C}^{18}\text{O}$  data. The de-blending limit is usually a good deal higher for crowded fields. However, using the present data set, this gives, for 0.11 K rms on the  $T_{\text{MB}}$  scale, a completeness level given by:

$$F = n_{bm} n_{\sigma} \Delta S_{rms} \Delta v PS_{jcm} \quad (12)$$

where  $n_{bm}$  is the number of beams (taken to be 2 in the present case),  $n_{\sigma}$  is the signal-to-noise (taken to be  $3\sigma$ ),  $\Delta S_{rms}$  is the rms noise level in a  $0.1 \text{ km s}^{-1}$  channel,  $\Delta v$  is the channel width used in the *CPROPS* analysis ( $0.1 \text{ km s}^{-1}$ ), and  $PS_{jcm}$  is the point source sensitivity of the JCMT ( $20.4 \text{ Jy K}^{-1} \text{ beam}^{-1}$ ). In practice  $n_{bm}$  and  $n_{\sigma}$  are both based on the *CPROPS* source identification parameters that are used, and for the present case Equations 11 and 12 then lead to a clump mass completeness of 0.15–0.2  $M_{\odot}$ .

The positions of the molecular  $\text{C}^{18}\text{O}$  clumplets reported in Table 5 were compared with the seventy-two  $850 \mu\text{m}$  submm clumps reported by Simpson et al. (2008). Of the 105 molecular clumplets, eighteen cross matched with the locations of submm clumps to within  $15''$ , with the majority of these agreeing to better than  $10''$ . The dust continuum masses and the gas virial mass estimates in these cases agreed to within factors of  $\sim 5$  of each other. However, the majority of clumplets do not positionally correlate with the submm clumps, and we have to surmise that the clumplets predominantly trace a different population of material from those exhibiting detectable  $850 \mu\text{m}$  emission in the Simpson et al. (2008) survey.

The thermal properties of the various clumplets detected using *CPROPS* are shown in Figure 16, which compares the clump excitation temperatures estimated from the  $\text{CO}$ ,  $^{13}\text{CO}$  and  $\text{C}^{18}\text{O}$  lines, after correcting the observed antenna temperatures to main beam brightness temperature. Figure 16 shows that the inferred  $\text{CO}$  excitation tem-

**Table 5.** The clumplet catalogue (a full version is available in the Supplementary material on-line). The clumplets listed in the catalogue are: (1) a short form running number, (2,3) Right Ascension and Declination (J2000) of the clump centre, (4,5,6) the major and minor axis of the clump deconvolved from the beam in arc seconds, along with the position angle (measured east of north), (7) the deconvolved radius of the clump as defined by Rosolowsky et al. (2006), (8,9) centre  $v_{LSR}$  and dispersion of the clump as determined from the  $C^{18}O$  data, (10) The virial mass, and (11) the Luminous mass estimated from the CO observations.

No	RA (J2000) h:m:s	Dec (J2000) d:m:s	Maj "	Min "	Pos angle (6)	Radius pc (7)	Velocity km s <sup>-1</sup> (8)	Dispersion km s <sup>-1</sup> (9)	Virial mass $M_{\odot}$ (10)	Luminosity K km s <sup>-1</sup> pc <sup>-2</sup> (11)
(1)	(2)	(3)	(4)	(5)	(6)	(7)	(8)	(9)	(10)	(11)
1	16:25:54.0	-24:29:46.7	22.9	16.1	51	0.02	2.95	0.20	0.71	0.00141
2	16:25:55.4	-24:17:30.2	7.9	7.7	-38	0.00	3.54	0.11	0.04	0.00015
3	16:25:56.9	-24:23:25.3	12.8	11.2	-41	0.01	3.45	0.17	0.27	0.00034
4	16:26:00.1	-24:31:24.7	42.1	13.2	2	0.02	3.41	0.28	1.62	0.00147
5	16:26:00.4	-24:33:53.0	8.4	8.0	63	0.00	3.69	0.17	0.13	0.00022
6	16:26:01.3	-24:32:29.1	26.6	14.2	132	0.02	3.35	0.26	1.18	0.00146
7	16:26:02.1	-24:18:45.2	11.0	27.2	65	0.01	3.75	0.32	1.51	0.00781
8	16:26:02.5	-24:25:31.2	13.6	12.4	118	0.01	2.92	0.23	0.56	0.00058
9	16:26:03.6	-24:34:24.0	12.1	10.2	118	0.01	3.49	0.15	0.19	0.00073
10	16:26:07.6	-24:19:29.4	87.7	18.3	29	0.04	3.88	0.18	1.24	0.01231

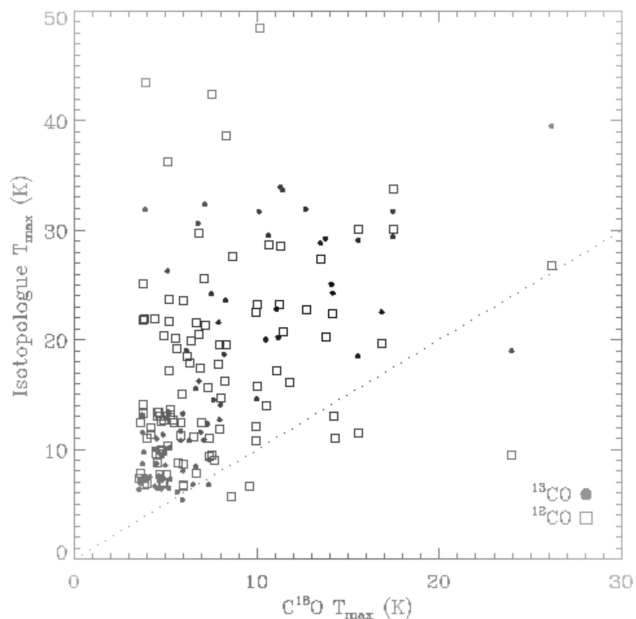


**Figure 16.** The clumplet excitation temperatures estimated from the CO and  $^{13}CO$  lines.

temperatures are generally higher than those inferred from the  $C^{18}O$  main beam brightness temperatures. This implies that the  $C^{18}O$  isotopologue may not be fully thermalised, as is consistent with the spectral profiles shown in Figure 6, or alternatively that the emission is clumpy on sub-beam scales, leading to a reduction in intensity as a consequence of a filling factor that is less than unity.

The Larson relations (Larson 1981) were used to examine the line width-size relation ( $\sigma \propto R^{\alpha}$ ), which relates the turbulent velocity dispersion of a structure to its size via a power law. Although the Larson relationships are known to trace the large-scale turbulent properties of molecular clouds, they may break down on smaller scales due to the increasing dominance of gravity and the transition to coherent (subsonic) linewidths (Goodman et al. 1998).

The velocity dispersion obtained from the data is plot-

ted as a function of clumplet radius in Figure 17. This can relate the properties of the very small clumplets characterised in this study to those of larger clouds elsewhere in the Galaxy. Although this relationship has been extensively characterised with observations of other molecular clouds, these generally sample clumps with higher radii and dispersion values, and so the current data extend previous work to much smaller size scales. Although the present data show considerable scatter, the smaller clouds appear consistent with that expected for a thermal component  $\leq 15$  K. Despite the fact that the *CPROPS* analysis may still suffer from systematic biases remaining in the technique, Figure 17 suggests that the smaller clumplets may be cooler (as they fall below the predicted 15 K thermal linewidth curve), although about half of the larger clumplets may be more consistent with temperatures in the range 20-30 K. Such a temperature spread is consistent with results in Orion A presented for an ensemble of clumps by Buckle et al. (2012). To determine the velocity dispersion, we adopt the following relationship:

$$\sigma_{tot} = \sqrt{\sigma_{nt}^2 + \sigma_o^2(\mu)} \quad (13)$$

where  $\sigma_{nt}^2$  and  $\sigma_o^2(\mu)$  are the non-thermal and thermal linewidths respectively, with the thermal component being given by:

$$\sigma_o^2(\mu) = \sqrt{\frac{kT}{\mu m_H}} \quad (14)$$

with  $m_H$  the mass of a hydrogen atom, and  $\mu$  the mean molecular weight of  $C^{18}O$  ( $\mu = 30$ ).

The data are over-plotted with curves showing the expected variation with  $\sigma_o$  for values of 0 and 15 K. The data are broadly consistent with this range, given that there will naturally be a spread in the gas temperatures from clump to clump. In general the size-line width trend observed is consistent with the standard GMC based size-line width relationship, with the clumplets having higher line widths as showing a similar trend to higher pressure regions of the galaxy.

The correlation between the dynamical (virial) and luminous masses of the molecular clumplets is examined in

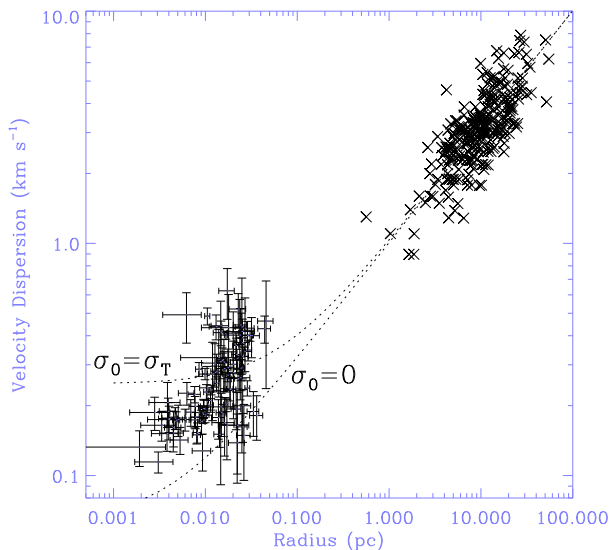


**Figure 17.** Velocity dispersion-size relationship of the molecular clumplets identified using *CPROPS*, shown as error bars on the left of the plot. The clumplet radii were estimated as described by Rosolowsky & Leroy (2006), and have been deconvolved from the telescope beam. The crosses on the right-hand side of the plot are values taken from the Solomon et al. (1987) survey of 273 clouds in the Galactic Plane, which showed that these clumps followed a Larson relationship. The two dotted curves show the expected values for the cases where the thermal linewidth,  $\sigma_0$  is set equal to zero, and for an example curve for a kinetic temperature of 15 K, chosen to be representative of cloud material. At larger values of radii and dispersion, these two curves approach each other, joining to the Solomon et al. clouds, and showing (despite some scatter that most plausibly may be a consequence of temperature variations in the clumps) that the Oph clumplets follow extrapolation of the Larson relationship to clump radii below 0.01 pc, when thermal linewidths start to become significant compared to the velocity dispersion. Although the uncertainties are relatively large, many of the Oph CO clumplets have dispersions close to the expected thermal linewidths for temperatures  $\sim 15$  K.  $\sigma_{nt}^2$  is therefore always less than  $0.1 \text{ km s}^{-1}$ , which is negligible compared to the *average* velocity dispersion of  $\text{C}^{18}\text{O}$  in Ophiuchus, which is  $\sim 0.8 \text{ km s}^{-1}$ . This is similar to that inferred for the W51 clump sample (Parsons et al. 2012), and slightly lower than the mean value inferred for clumps toward Orion A (Buckle et al. 2012).

Figure 18. Although many of the points whose virial masses are below  $\sim 1 M_\odot$  have relatively large uncertainties (see Section 6 for discussion of s/n limitations), these points have been left on Figure 18 with their mean values indicated by filled circles as they do appear to follow the trend. The luminosity for the x-axis and the sizes and linewidths that contribute to the virial mass are all deduced by moments of the intensity distribution. These moments have been extrapolated down to their expected values in the absence of noise (as described by Rosolowsky & Leroy 2006). To assess the significance of an error bar, the intensity distribution (i.e. a set of  $(x, y, v, T_a^*)$  data) was sampled with replication to draw the same number of points from the data as in the original clump, thus enabling extrapolation of the points down to the zero level. This is a ‘bootstrap’ approach, which has

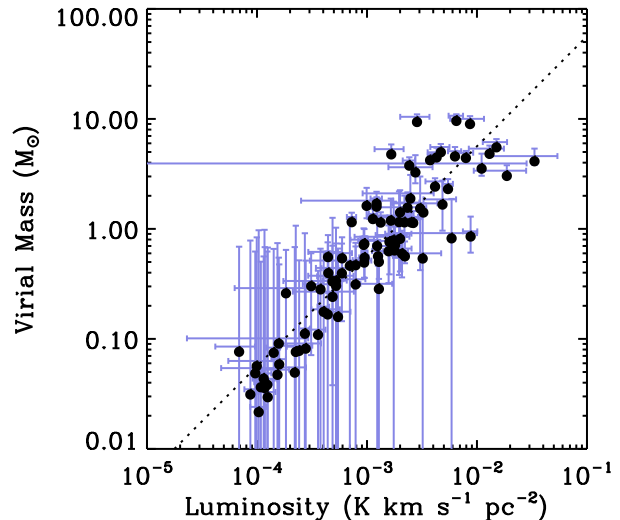


**Figure 18.** Virial masses (in  $M_{\text{sun}}$ ) of the molecular clumplets identified by *CPROPS* plotted against the CO luminosity (in  $\text{K km s}^{-1} \text{ pc}^2$ ). The dotted line shows that expected if  $M_{\text{vir}} = M_{\text{lum}}$  using a CO-to- $\text{H}_2$  conversion factor of  $4.95 \times 10^{22} \text{ cm}^2 (\text{K km s}^{-1})^{-1}$ , which is established as the line that goes through those points. The clumplets detected here follow a continuous relationship, that with other data in the literature extends over almost 9 orders of magnitude in our own Galaxy, and extends out to local group galaxies with appropriate scaling of  $X_{\text{CO}}$  for metallicity (Bolatto et al. 2008, Hughes et al. 2010).

been theoretically justified as an empirical estimate of uncertainties given a set of measurements (Efron 1979). This procedure was repeated 1000 times for each clump and the error distribution measures the width of the resulting distribution of samples. This method has been shown in practice to do a good job in assessing the uncertainties from noise in the data and from the extrapolation process. It is however less good at assessing the systematic errors engendered by the cataloguing method itself, which is a more difficult problem to solve rigorously. On Figure 18, those points falling above the dotted line are most likely gravitationally unbound or pressure confined, whereas those falling below the dotted line may be self-gravitating. Despite the rather large uncertainties, it does appear that at least some of the identified clumplets may be able to collapse to form stars.

Figure 18 shows an approximately linear correlation between a dynamical estimate of the mass (i.e. the virial mass estimated assuming uniform density) compared to the luminosity of the line (Bolatto et al. 2008). Clumplets undergoing gravitational collapse would lie on the right-hand side of the dotted line, whereas pressure-confined or gravitationally unbound clumplets would lie to the left. The majority of the data points cluster closely to the line between these two constraints. Within the noise constraints, there are a small number of clumplets which may be in free-fall, as Simpson et al. 2011 have suggested), or alternatively may be pressure confined. Extrapolation of the dotted line to higher  $M_{\text{vir}}$  and luminosity ranges shows that this linear trend holds over 11 dex in luminosity (see for example Rebolledo et al. 2012).

## 7 SUMMARY

We have analysed JCMT Gould Belt survey CO,  $^{13}\text{CO}$  and  $\text{C}^{18}\text{O}$  3-2 maps of the main star-forming cloud in Ophiuchus LDN1688. Our main conclusions are:

(i) In Oph A, the typical integrated intensity ratios  $^{13}\text{CO}/\text{C}^{18}\text{O}$  range from  $\sim 2$ –7, corresponding to  $\tau(^{13}\text{CO})$  of 2–16 and  $\tau(\text{C}^{18}\text{O})$  of  $\sim 0.1$ –2.0.  $^{13}\text{CO}$  is usually found to be optically thick around the main clumps.  $\text{C}^{18}\text{O}$  is generally optically thin across 96 per cent of the whole area mapped, although does reach opacities up to 2 in several of the clumps. In particular the more abundant  $^{13}\text{CO}$  emission from the PDR region is self-absorbed with a  $^{13}\text{CO}/\text{C}^{18}\text{O}$  integrated intensity ratio as low as 1.2.

(ii) From the isotopomeric lines, the gravitational binding energy is estimated to be  $4.5 \times 10^{39}$  J ( $3497 M_{\odot} \text{ km}^2 \text{ s}^{-2}$ ).

(iii) The velocity structure in the gas around protostars originally detected by the *Spitzer* c2d survey data were examined. Outflows were detected towards 28 out of 30 sources (8 firm associations, with 20 more marginal). Several new sources identified in the c2d survey have evidence for red and/or blueshifted outflow lobes, and it is less likely that flat spectrum objects have firm outflow detections than is the case for Class 0/I protostars.

(iv) After inclination and optical depth are corrected for, the total outflow kinetic energy is  $1.3 \times 10^{38}$  J ( $67 M_{\odot} \text{ km}^2 \text{ s}^{-2}$ ) corresponding to 21 per cent of the turbulent kinetic energy. This suggests that outflows are significant, but *not* the dominant source of turbulence in Ophiuchus.

(v) The turbulent energy is estimated to be  $6.3 \times 10^{38}$  J ( $3497 M_{\odot} \text{ km}^2 \text{ s}^{-2}$ ), which is roughly a factor of 7 times smaller than the binding energy, suggesting both that the cloud as a whole is gravitationally bound, and also that the outflows are not the dominant source of turbulent injection into the Oph cloud.

(vi) That the turbulent kinetic energy is too small to support the cloud, and the outflow kinetic energy is insufficient to be the dominant driver of turbulence (since the outflows are also unable to support the cloud), leads to the inevitable conclusion that on the large scale, the Ophiuchus cloud is in a state of collapse.

(vii) 105 clumplets were detected within the cloud using the *CPROPS* source extraction algorithm, whose radii ranged from 0.01–0.05 pc, and which had virial masses between 0.1 and  $12 M_{\odot}$ , and luminosities between 0.001 and  $0.1 \text{ K km s}^{-1} \text{ pc}^{-2}$ . Eighteen of these lay within one beamwidth of a submm 850  $\mu\text{m}$  core.

(viii) The excitation temperatures of the clumplets ranged from 10–50 K, with the majority of the warmest clumplets being associated with the Oph A region, and from close to the PDR.

(ix) From the velocity dispersion–radius plot, the expected variation is well fitted for clumplets having a typical temperature of  $\sim 10$ –25 K, with the  $\sigma_o$  set equal to zero, or to its thermal width. In general the size–line width trend observed is consistent with the standard GMC based size–line width relationship, with the clumplets having lower line widths than that of larger molecular clouds.

(x) Comparison between the virial mass, as a dynamical estimate of the masses of individual clumplets, and the luminosity of the cloud clumplet ensemble shows a good cor-

relation consistent with a  $\text{C}^{18}\text{O}$ -to- $\text{H}_2$  conversion factor of  $4.95 \times 10^{22} \text{ cm}^2 / \text{K km s}^{-1}$ , although a small number of clumplets may either be in free-fall, or be pressure confined.

## 8 ACKNOWLEDGEMENTS

We thank Alain Abergel for sharing his archival ISOCAM data at an early stage of writing this paper. The JCMT is operated by the Joint Astronomy Centre, Hawaii, on behalf of the UK STFC, the Netherlands NWO and the Canadian NRC. We gratefully acknowledge the support of the JCMT staff and operators.

## REFERENCES

- Abergel, A., Bernard, J.P., Boulanger, F., Cesarsky, C., Desert, F. X., Falgarone, E., Lagache, G., Perault, M. al 1996, *A&A*, 315, L329  
 Allen D.A., 1972, *ApJL*, 172, L55  
 Allen, L.E., Myers, Philip C., Di Francesco, J., Mathieu, R., Chen, H., Young, E., 2002, *ApJ*, 566, 993  
 Allen, P.R., Koerner, D.W., Reid, I.N. Trilling, D.E., 2005, *ApJ*, 625, 385  
 Alves, J., Lombardi, M., Lada, C.J., 2007, *A&A*, 462, L17  
 Andr $\acute{a}$ cuterme, P., Martin-Pintado, J., Despois, D., & Montmerle, T., 1990, *A&A*, 236, 180  
 Andr $\acute{a}$ rmacut $\acute{e}$ e, P., Montmerle, T., Feigelson, E.D., Steppe, H., 1990, *A&A*, 240, 321  
 Andr $\acute{a}$ rmacut $\acute{e}$ e, P., Ward-Thompson, D., Barsony M., 1993, *ApJ*, 406, 122  
 Andr $\acute{a}$ rmacut $\acute{e}$ e, P., Ward-Thompson, D., Barsony M., 2000, *Protostars and Planets IV*, p. 59  
 Arab, H., Abergel, A., Habart, E., Bernard-Salas, J., Ayasso, H., Dassas, K., Martin, P.G., White, G.J. 2012, *A&A*, 541, A19  
 Avery, L.W., Hayashi, S.S. & White, G.J., 1990, *ApJ*, 357, 524  
 Beckford, A.F., Lucas, P.W., Chrysostomou, A.C., Gledhill, T.M., 2008, *MNRAS*, 384, 907  
 Bernard-Salas, J., Habart, E., Arab, H. al, 2012, *A&A*, 538, A37  
 Bertoldi, F., McKee, C.F., 1992, *ApJ*, 395, 240  
 Blake, G.A., Sutton E. C., Masson C. R., Phillips T. G., 1987, *ApJ*, 315, 621  
 Blitz, L., & Thaddeus, P., 1980, *ApJ*, 241, 676  
 Bolatto, A.D., Leroy, A.K., Rosolowsky, E., Walter, F. & Blitz, L., 2008, *ApJ*, 686, 948  
 Bontemps, S., Andr $\acute{a}$ rmacut $\acute{e}$ e P., Kaas A A., Nordh L., Olofsson G., Hultgren M., Abergel A., Blommaert J., Boulanger F., Burgdorf, M., Cesarsky C. J., 2001, *A&A*, 372, 173  
 Bontemps, S., Andre P., Terebey S., Cabrit S., 1996, *A&A*, 311, 858  
 Bontemps S., Andre P., 1997, in Reipurth B., Bertout C., eds, *Herbig-Haro Flows and the Birth of Stars Vol. 182 of IAU Symposium, An asymmetric radio continuum HH-jet from VLA1623*. p. 63P  
 Boogert, A.C.A., Hogerheijde, M.R., Ceccarelli, C., Tielens, A.G.G.M., van Dishoeck, E.F., Blake, G.A., Latter, W.B., Motte, F., 2002, *ApJ*, 570, 708

Buckle, J.V., Curtis E.I., Roberts J.F., White G. J., Hatchell J., Brunt C., Butner H. M., Cavanagh B., Chrysostomou A., Davis C.J., Duarte-Cabral A., Etxaluze M., di Francesco J., 2010, MNRAS, 401, 204  
 Buckle, J.V al, 2009, MNRAS, 399, 1026  
 Buckle, J.V al, 2010, MNRAS, 401, 204  
 Buckle, J.V., Davis, C.J., Francesco, J. Di, al, 2012, MNRAS, 422, 52  
 Bussmann, R. S., Wong T. W., Hedden A. S., Kulesa C. A., Walker C. K., 2007, ApJL, 657, L33  
 Caratti o Garatti, A., Giannini, T., Nisini, B., Lorenzetti, D., 2006, A&A, 459, 821  
 Casassus, S., Dickinson, C., Cleary, K., Paladini, R., Etxaluze M., Lim T., White, G J., Burton, M., Indermuehle, B., Stahl, O., Roche, P., 2008, MNRAS, 391, 1075  
 Castellanos, P., Casassus, S., Dickinson, C., Vidal, M., Paladini, R., Cleary, K., Davies, R.D., Davis, R.J. al, 2011, MNRAS, 411, 1137  
 Ceccarelli, C., Caux, E., White, G.J., Molinari, S. al, 1998, A&A, 331, 372  
 Chabrier, G. 2003, PASP, 115, 763  
 Chapman, N.L., Mundy, Lee G., Lai, Shih-Ping, Evans, N., 2009, ApJ, 690, 496  
 Chen, H., Grenfell T.G., Myers P.C., Hughes J.D., 1997, ApJ, 478, 295  
 Chen, H., Myers, P.C., Ladd, E.F., Wood, D.O.S., 1995, ApJ, 445, 377  
 Comeron, F., Rieke G. H., Burrows A., Rieke M. J., 1993, ApJ, 416, 185  
 Christie, H., Viti, S., Yates, J. et al., 2012, MNRAS, 422, 968  
 Curtis, E.I., Richer, J.S., Buckle, J., 2009, MNRAS, 401, 455  
 Curtis, E.I., Richer J.S., Swift J.J., Williams J.P., 2010, MNRAS, 408, 1516  
 Davis, C.J. & Eislrmddotoffel, J., 1995, A&A, 300, 851  
 Davis, C.J., Gell, R., Khanzadyan, T., Smith, M.D. and Jenness, T., 2010, A&A, 511, A24  
 Dent, W.R.F., Matthews, H.E., & Walther, D.M., 1995, MNRAS, 277, 193  
 Dent, W.R.F., Clarke C., 2005, in Protostars and Planets V, A Survey for Molecular Gas Around Evolved Classical T Tauri Stars. p. 8435  
 Dickinson, C., Davies, R.D., Allison, J.R., Bond, J.R., Casassus, S., Cleary, K., Davis, R.J., Jones, M.E. al, 2009, ApJ, 690, 1585  
 Duchrmhatene, G., Bouvier, J., Bontemps, S., Andrrmacutee, Motte, F., 2004, A&A, 427,651  
 Efron, B. 1979, Ann.Statistics, 7, 1  
 Elias, J. H., 1978, ApJ, 224, 453  
 Enoch, M. L., Evans II N. J., Sargent A. I., Glenn J., 2009, ApJ, 692, 973  
 Enoch, M.L.; Evans, N.J., Sargent, A.I., G,J. al, 2008., ApJ, 684, 1240  
 Evans, N. J., Dunham M. M., Jorgensen J. K., Enoch M. L., Meracuttein B., van Dishoeck E.F., Alcalacuterma, J.M., Myers P. C., Stapelfeldt K.R., 2009, ApJS, 181, 321  
 Fridlund, C.V.M. & White, G.J., 1989, A&A, 223, L13  
 Fridlund, C.V.M., Bergman, P., White, G.J., Pilbratt, G.L., Tauber, J. A., 2002, A&A, 382, 573  
 Fridlund, C.V.M., Liseau, R., Djupvik, A.A., Hultgren, M., White, G.J., Favata, F., Giardino, G., 2005, A&A, 436, 983  
 Friesen, R. K., Di Francesco, J., Shirley, Y.L., Myers, P.C., 2009, ApJ, 697, 1457  
 Frerking, M. A., Langer W. D., Wilson R. W., 1982, ApJ, 262, 590  
 Giannini, T., Nisini B., Lorenzetti D., 2001, ApJ, 555, 40  
 Gacutermomez, M., Stark, D.P., Whitney, B.A. & Churchwell, E., 2003, AJ, 126, 863  
 Gacutermomez, M., Whitney, B.A., & Wood, K., 1998, AJ, 115, 2018  
 Goodman, A.A., Barrance J.A., Wilner D.J., Heyer M.H., 1998, ApJ, 504, 223  
 Grasdalen, G.L., Strom, K.M., Strom, S.E., 1973, ApJL, 184, L53  
 Graves, S.F., Richer J.S., Buckle J.V., Duarte-Cabral A., 2010, MNRAS, 409, 1412  
 Greene, T.P., Wilking, B.A.; Andre, P., Young, E.T. al, 1994, ApJ, 434, 614  
 Greene, T.P., Meyer, M.R., 1995, ApJ, 450, 233  
 Grosso, N., Alvacutees, J., Neuhrmddotauer, R., & Montmerle, T., 2001, A&A, 380, L1  
 Habart, E., Boulanger, F., Verstraete, L., Pineau des Foracuttees, G., Falgarone, E., Abergel, A., 2003, A&A, 397, 623  
 Habart, E., Dartois, E., Abergel, A., al, 2010, A&A, 518, L116  
 Habart, E., Abergel, A., Boulanger, F., Joblin, C., 2011, A&A, 527, A122  
 Haisch Jr., K. E., Barsony M., Ressler M. E., Greene T. P., 2006, AJ, 132, 2675  
 Harju, J., Juvela, M., Schlemmer, S., Haikala, L. K., 2008, A&A, 482, 631  
 Hatchell, J., Fuller G.A., Ladd E.F., 1999a, A&A, 344, 687  
 Hatchell, J., Roberts H., Millar T.J., 1999b, A&A, 346, 227  
 Hatchell, J., Fuller G.A., Richer J. S., 2007, A&A, 472, 187  
 Hatchell, J., Terebey, S., Huard, T., Mamajek, E., al, 2012, ApJ, 754, 104  
 Hennebelle, P. & Chabrier, G., 2008, ApJ, 684, 395  
 Hennebelle, P., Chabrier, G., 2011, ApJ, 743, L29  
 Hocuk, S., Spaans, M. 2010, A&A, 510, A110  
 Hughes, A. al, 2010, MNRAS, 406, 2065  
 Imai, H., Nakashima, K., Bushimata, T., Choi, Y.K., al, 2007, PASJ, 59, 1107  
 Johnstone, D., Wilson, C.D., Moriarty-Schieven, G., al, 2000, ApJ, 545, 327  
 Jorgensen, J.K., Johnstone, D., Kirk, H., Myers, P.C., al, 2008, ApJ, 683, L187  
 Jorgensen J.K., van Dishoeck E.F., Visser, R., Bourke, T.L., Wilner D.J., Lommen D., Hogerheijde M.R., Myers P.C., 2009, A&A, 507, 861  
 Kamazaki, T., Saito, M., Hirano, N., Kawabi, R., al 2001, ApJ, 548, 278  
 Kamazaki, T., Saito, M., Hirano, N., Umamoto, T., al 2003, ApJ, 584, 357  
 Kamegai, K., Ikeda, M., Maezawa, H., I., Tetsuya., I al 2003, ApJ, 589, 378  
 Khanzadyan, T., Gredel, R., Smith, M. D., Stanke, T., 2004, A&A, 426, 171  
 Kramer, C., Stutzki, J., Rohrig, R., Corneliussen, U.

- 1998, *A&A*, 329, 249
- Kroupa, P., 2002, *ASPC*, 285, 86
- Kryukova, E., Megeath, S.T., Gutermuth, R.A., Pipher, J., Allen, T.S., Allen, L.E., Myers, P.C., Muzerolle, J., 2012, *AJ*, 144, 31
- Kulesa, C.A., Hungerford, A.L., Walker, C.K., Zhang, X. al, 2005. *ApJ*, 625, 194
- Kutner, M.L., Ulich, B.L., 1981, *ApJ*, 250, 341
- Ladd, E.F., 2004, *ApJ*, 610, 320
- Larsson al, 2007, *A&A*, 466,999
- Ladd, E.F., Fuller G.A., Deane J R., 1998, *ApJ*, 495, 871
- Larson, R.B. 1981, *MNRAS*, 194, 809
- Lee, M-Y., Stanimirovir*macutec*, S., Wolfire, M.G., Shetty, R., Glover, S., Molina, F., Leseen, R. 2014, preprint (arXiv 1401.5117)
- Leous,J.A., Feigelson,E.D., Andre,P., Montmerle,T., 1991, *ApJ*, 379, 683
- Liseau, R., Goldsmith, P.F., Larsson, B., Pagani, L., al, 2012, *A&A*, 541, A73
- Liseau, R., Justtanont, K., 2009, *A&A*, 499,799
- Liseau, R., Larsson, B., Brandeker, A., Bergman, P., al, 2003, 402, L73
- Liseau, R., Larsson, B., Bergman, P., Pagani, L., Black, J.H., Hjalmarson, *angstrom.*, Justtanont, K., 2010, *A&A* 510, A98
- Liseau, R., White, G. J., Larsson, B., Sidher, S., 1999a, *A&A*, 344, 342
- Liseau, R.; White, G. J.; Larsson, B., 1999b, *The Universe as Seen by ISO*. Eds. P. Cox & M.F. Kessler., *ESA-SP 427.*, p. 703
- Loinard, L., Chandler, C.J.; Rodriguez,L.F., D'Alessio, P., al, 2007, *ApJ*, 670, 1353
- Loinard, L., Torres, R.M., Mioduszewski, A.J. & Rodriguez, Luis F., 2008, *ApJ*, 675, L29
- Loinard, L., Zapata, L.A., Rodrguac*uteec*, L.F. al., 2013, *MNRAS*, 430, L10
- Lombardi, M., Lada, C.J., Alves, J., 2008, *A&A*, 489, 143
- Loren, R.B. al, 1989a, *ApJ* 338, 902
- Loren, R.B. al, 1989b, *ApJ*, 338, 925
- Loren, R.B., Wootten, A., & Wilking, B. A., 1990, *ApJ*, 365, 269
- Luhman, K.L., Rieke, G.H., 1999, *ApJ*, 525, 440
- Maruta, H., Nakamura, F., Nishi, R., Ikeda, N., al 2010, *ApJ*, 714, 680
- Minchin, N.R., White, G.J., 1995, *A&A*, 302, L25
- Miville-Desch*hatenes*, M.-A, Martin, P. G., Abergel, A., Bernard, J.-P., Boulanger, F., Lagache, G., Anderson, L. D., *Andracutee*, P. al, 2010, *A&A*, 518, L104
- Molinari, S. al 2000, *ApJ.*, 538, 698
- Motte, F., *Andrrmacutee*, P. & Neri, R., 1998, *A&A*, 336, 150
- Myers, P.C., Ladd E.F., 1993, *ApJL*, 413, L47
- Murillo, N.M., Lai S.-P., 2013, *ApJL*, 764, L15
- Nakamura, F., Kamada, Y., Kamazaki, T., Kawabe, R., Kitamura, Y., Shimajiri, Y., Tsukagoshi, T., Tachihara, K., Akashi, T., Azegami, K., Ikeda, N., Kurono, Y., Li, Z., Miura, T., Nishi, R., Umemoto, T., 2011, *ApJ*, 726, 46
- Narayanan, G. & Logan, D.W., 2006, *ApJ*, 647, 1170
- Naylor, D. A., Dartois, E., Habart, E., al, 2010, *A&A*, 518, L117
- Nisini, B., Benedettini, M., Giannini,T., Codella,C., Lorenzetti,D., di Giorgio,A.M., Richer,J.S., 2000, *A&A*, 360, 297
- Padgett, D.L., Rebull, L.M., Stapelfeldt, K.R., Chapman, N.L., Lai S.-P., Mundy L.G., Evans II N.J., Brooke,T.Y., Cieza L.A., Spiesman W.J., Noriega-Crespo A.,McCabe C.E., Allen L.E., 2008, *ApJ*, 672, 1013
- Palmeirim, P. al 2013, *A&A*, 550, A38
- Papadopoulos, P.P., van der Werf, P.P., Xilouris, E.M., Isaak, K.G., Gao, Y., M'uhle, S., 2012a, *MNRAS*, 426, 2601
- Papadopoulos, P.P., van der Werf, P.P., Xilouris, E.M., Isaak, K.G., Gao, Y., 2012b, *ApJ*, 751, 10
- Parsons, H., Thompson, M.A., Clark, J.S., Chrysostomou, A., 2012, *MNRAS*, 424, 1638
- Pekruhl, S., Preibisch, T., Schuller, F., Menten, K., 2013, *A&A*, 550, A29
- Pineda, J.E., Rosolowsky, E.W., Goodman, A.A. 2009, *ApJL*, 699, L134
- Peretto, N., Fuller, G.A., 2010, *ApJ*, 723, 555
- Phelps, R. L. & Barsony, M., 2004, *AJ*, 127, 420
- Phillips, J.P., White, G.J., Ade, P.A.R., Cunningham, C.T., Richardson, K.J., Robson, E.I., Watt, G.D., 1982, *A&A*, 116, 130
- Phillips, J.P., White, G.J., Rainey, R., Avery, L.W., Richardson, K.J., Griffin, M.J., Cronin, M.J., Monteiro, T., Hilton, J., 1988, *A&A*, 190, 289
- Rainey, R., White, G.J., Richardson, K.J., Griffin, M.J., Cronin, N.J., Monteiro, T.S., Hilton, J., 1987, *A&A*, 179, 237
- Ratzka, T. *Kddotohler*, R. & Leinert, Ch., 2005, *A&A*, 437, 611
- Rawlings, M. G., Juvela, M., Lehtinen, K., Mattila, K., Lemke, D., 2013, *MNRAS*, 428, 2617
- Rebolledo, D., Wong, T., Leroy, A., Koda, J., Meyer, J.D., 2012, *ApJ*, 757, 155
- Richardson, K.J., White, G.J., Avery, L.W., Lesurf, J.C.G., Harten, R. H., 1985, *ApJ*, 290, 637
- Ridge, N. A. al, 2006, *AJ*, 131, 2921
- Rohlfs, K., Wilson T. L., 2000, *Tools of Radio Astronomy*
- Rosolowsky, E., Leroy,A., 2006, *PASP*, 118, 590
- Schmeja, S., Kumar, M.S.N. & Ferreira, B., 2008, *MNRAS*, 389, 1209
- Scoville, N.Z., Yun, M.S., Sanders, D.B., Clemens, D.P., Waller, W.H., 1987, *ApJS*, 63, 821
- Sekimoto, Y., Tatematsu K., Umemoto T., Koyama K., Tsuboi Y., Hirano N., Yamamoto S., 1997, *ApJ*, 489, L63
- Simpson, R. J., Nutter, D., Ward-Thompson, D., 2008, *MNRAS*, 391, 205
- Simpson, R. J., Johnstone,D., Nutter, D., Ward-Thompson, D., Whitworth, A.P., 2011, *MNRAS*, 417, 216
- Smith, M.D., Gredel, R., Khanzadyan, T., Stanke, T. al, 2005, *Mem della Soc Astronomica Italiana*, 76, 247
- Snow, T.P., Destree, J.D., Welty, D.E., 2008, *ApJ*, 679, 512
- Solomon, P.M., Rivolo, A.R., Barrett, J., & Yahil, A., 1987, *ApJ*, 319, 730
- Stamatellos, D., Whitworth, A.P. & Ward-Thompson, D., 2007, *MNRAS*, 379, 1557
- Starck, J-L., Murtagh, F. 2006, *Astronomical Image and Data Analysis*, *Astronomy and Astrophysics Library*. Springer-Verlag Press

- Tachihara, K., Mizuno A., Fukui Y., 2000, ApJ, 528, 817  
Tamura, M., Sato, S., Kaifu, N., Hough, J.H., & Suzuki, H., 1990, ApJ, 350, 728  
Terebey, S., Vogel, S.N., & Myers, P.C., 1989, ApJ, 340, 472  
Thompson, M.A., White, G.J., Morgan, L.K., Miao, J., Fridlund, C.V.M., Hultgren-White, M., 2004, A&A, 414, 1017  
van der Marel, N., Kristenses, L.E., Visser, R., Mottram, J., Yildiz, U.A., van Dishoeck, E.F., 2013, A&A, 556, A76  
van Kempen, T.A., van Dishoeck, E.F., Salter, D.M., Hogerheijde, M.R., Jorgensen, J.K., Boogert, A. C.A., 2009, A&A, 498, 167  
Ward-Thompson, D. al, 2007, PASP, 119, 855  
Ward-Thompson, D., Kirk J. M., Greaves J. S., *Andrrmacutee*, P., 2011, MNRAS, 415, 2812  
White, G.J., al, 2000, A&A, 364, 741  
White, G.J., Phillips, J.P., Richardson, K.J., Harten, R.H., 1986, A&A, 159, 309  
White, G.J., Araki, M., Greaves, J. S., Ohishi, M., Higginbottom, N. S., 2003, A&A, 407, 589  
White, G.J., Fridlund, C.W.M., Bergman, P., Beardsmore, A., Liseau, R., Price, M., Phillips, R.R. 2006, ApJ Lett, 651, L41  
White, G.J., Rainey, R., Hayashi, S.S., Kaifu, N., 1987, A&A, 173, 337  
White, G.J., Sandell, G., 1995, A&A, 299, 179  
Wilking, B.A. & Lada, C. J., 1983, ApJ, 274, 698  
Wilking, B.A., Claussen, M.J., 1987, ApJL, 320, L133  
Wilking, B.A., Lada, C.J., Young, E.T., 1989, ApJ, 340, 823  
Wilking, B.A., Schwartz, R.D., Fanetti, T.M., & Friel, E.D., 1997, PASP, 109, 549  
Wilking, B.A., Bontemps, S., Schuler, R.E., Greene, T.P., *Andrrmacutee*, P., 2001, ApJ, 551, 357  
Wilking, B.A., Gagne, M., Allen, L.E. 2008, Handbook of Star Forming Regions, Volume II: The Southern Sky ASP Monograph Publications, Edited by Bo Reipurth, p.351  
Wilson, T.L., Rood R., 1994, ARAA, 32, 191  
Wouterloot, J. G. A., Brand, J. & Henkel, C., 2005, A&A, 430, 549  
Wu, J., Wang, M., Yang, J., Deng, L., & Chen, J., 2002, AJ, 123, 1986  
Ybarra, J.E., Barsony M., Haisch Jr. K.E., Jarrett T.H., Sahai, R., Weinberger, A.J., 2006, ApJ, 647, L159  
Young, K.E. Enoch, M.L., Evans, N.J., Glenn, J., al, 2006, ApJ, 644, 326  
Zavagno, A., Russeil, D., Motte, F., Anderson, L. D., Deharveng, L., *Rodacuteton*, J. A., Bontemps, S., Abergel, A., al 2010, A&A, 518, L81  
Zhang, M. & Wang, H., 2009, ApJ, 138, 1830  
Zhang, M., Brandner, W., Wang, H., Gennaro, M., Bik, A., Henning, Th., Gredel, R., Smith, M., Stanke, Th., 2013, A&A, 553, A41

Table 5: The clumplet catalogue. The clumplets listed in the catalogue are: (1) a short form running number, (2,3) Right Ascension and Declination (J2000) of the clump centre, (4,5,6) the major and minor axis of the clump deconvolved from the beam in arc seconds, along with the position angle (measured east of north), (7) the deconvolved radius of the clump as defined by Rosolowsky et al. (2006), (8,9) centre  $v_{LSR}$  and dispersion of the clump as determined from the  $C^{18}O$  data, (10) The virial mass, and (11) the Luminous mass estimated from the CO observations.

No	RA (J2000)	Dec (J2000)	Maj	Min	Pos angle	Radius	Velocity	Dispersion	Virial mass	Luminosity
(1)	h:m:s.s	d:m:s.s	"	"	(6)	pc	km s <sup>-1</sup>	km s <sup>-1</sup>	$M_{\odot}$	K km s <sup>-1</sup> pc <sup>-2</sup>
	(2)	(3)	(4)	(5)		(7)	(8)	(9)	(10)	(11)
1	16:25:54.0	-24:29:46.7	22.9	16.1	51	0.02	2.95	0.20	0.71	0.00141
2	16:25:55.4	-24:17:30.2	7.9	7.7	-38	0.00	3.54	0.11	0.04	0.00015
3	16:25:56.9	-24:23:25.3	12.8	11.2	-41	0.01	3.45	0.17	0.27	0.00034
4	16:26:00.1	-24:31:24.7	42.1	13.2	2	0.02	3.41	0.28	1.62	0.00147
5	16:26:00.4	-24:33:53.0	8.4	8.0	63	0.00	3.69	0.17	0.13	0.00022
6	16:26:01.3	-24:32:29.1	26.6	14.2	132	0.02	3.35	0.26	1.18	0.00146
7	16:26:02.1	-24:18:45.2	11.0	27.2	65	0.01	3.75	0.32	1.51	0.00781
8	16:26:02.5	-24:25:31.2	13.6	12.4	118	0.01	2.92	0.23	0.56	0.00058
9	16:26:03.6	-24:34:24.0	12.1	10.2	118	0.01	3.49	0.15	0.19	0.00073
10	16:26:07.6	-24:19:29.4	87.7	18.3	29	0.04	3.88	0.18	1.24	0.01231
11	16:26:09.3	-24:17:54.0	43.8	16.2	92	0.02	3.17	0.40	3.99	0.00440
12	16:26:09.9	-24:19:40.6	31.4	19.3	54	0.02	2.72	0.32	2.34	0.00532
13	16:26:10.1	-24:23:21.0	10.2	9.2	72	0.01	3.41	0.49	1.57	0.00073
14	16:26:10.9	-24:24:43.7	35.1	21.5	67	0.02	2.43	0.44	4.93	0.00334
15	16:26:12.2	-24:15:24.5	9.3	8.7	0	0.01	2.87	0.14	0.11	0.00027
16	16:26:12.3	-24:17:21.6	18.9	32.6	0	0.02	2.22	0.14	0.44	0.00457
17	16:26:12.4	-24:32:11.5	8.4	7.6	86	0.00	3.45	0.16	0.09	0.00028
18	16:26:13.3	-24:22:05.3	25.3	12.4	123	0.01	4.27	0.41	2.62	0.00094
19	16:26:13.9	-24:21:37.9	143.0	18.0	-26	0.05	3.20	0.46	10.19	0.00626
20	16:26:14.3	-24:25:10.7	7.9	8.5	73	0.00	4.46	0.21	0.17	0.00010
21	16:26:14.7	-24:25:34.2	57.2	39.6	61	0.04	3.21	0.43	8.46	0.00456
22	16:26:16.0	-24:14:50.8	8.2	8.0	33	0.00	2.68	0.15	0.09	0.00013
23	16:26:16.4	-24:23:57.6	18.8	11.0	102	0.01	4.06	0.20	0.48	0.00061
24	16:26:16.7	-24:25:31.3	25.8	11.2	3	0.01	2.49	0.18	0.46	0.00145
25	16:26:18.3	-24:14:24.4	11.0	7.5	17	0.00	3.04	0.15	0.11	0.00013
26	16:26:19.1	-24:22:39.5	48.9	16.5	-22	0.03	2.63	0.37	3.68	0.00564
27	16:26:20.8	-24:33:51.7	17.0	11.8	132	0.01	2.62	0.21	0.52	0.00093
28	16:26:21.7	-24:26:45.7	23.9	13.8	0	0.02	2.66	0.32	1.61	0.00101
29	16:26:21.9	-24:16:24.2	9.1	7.7	119	0.00	3.60	0.18	0.13	0.00018
30	16:26:22.4	-24:19:53.7	50.9	14.7	77	0.02	3.37	0.45	4.96	0.00526
31	16:26:23.5	-24:20:29.3	16.9	12.7	50	0.01	2.80	0.27	0.93	0.00143
32	16:26:25.9	-24:32:54.9	12.0	9.7	26	0.01	3.21	0.17	0.24	0.00046
33	16:26:26.1	-24:24:51.0	10.5	8.8	114	0.01	1.90	0.17	0.19	0.00025
34	16:26:27.6	-24:23:52.4	22.5	18.3	77	0.02	3.65	0.43	3.49	0.01874
35	16:26:27.7	-24:14:58.9	43.0	17.8	27	0.02	2.40	0.29	2.22	0.00312
36	16:26:27.8	-24:26:44.5	16.4	12.4	43	0.01	3.93	0.23	0.66	0.00072
37	16:26:28.4	-24:22:56.1	24.6	12.5	103	0.01	2.88	0.44	2.98	0.00975
38	16:26:31.2	-24:18:53.1	59.4	15.7	-19	0.03	3.03	0.43	5.22	0.00225
39	16:26:31.6	-24:18:42.0	25.1	16.1	-8	0.02	3.85	0.29	1.55	0.00162
40	16:26:32.2	-24:16:02.2	24.2	16.2	-6	0.02	3.17	0.62	7.02	0.00152
41	16:26:32.5	-24:26:17.1	62.4	19.7	54	0.03	2.76	0.40	5.30	0.01337
42	16:26:33.2	-24:24:16.3	17.4	9.3	30	0.01	2.81	0.13	0.16	0.00070
43	16:26:34.6	-24:28:08.8	61.6	13.8	33	0.03	2.66	0.39	4.04	0.00568
44	16:26:36.2	-24:17:58.5	32.5	22.3	-7	0.02	3.54	0.29	2.13	0.00396
45	16:26:36.9	-24:20:18.3	7.5	7.2	107	0.00	2.79	0.13	0.04	0.00029
46	16:26:39.7	-24:31:41.8	15.3	10.5	-8	0.01	2.93	0.19	0.38	0.00063
47	16:26:41.8	-24:24:02.7	12.3	8.8	-22	0.01	3.21	0.19	0.25	0.00041
48	16:26:41.8	-24:17:44.1	27.7	20.7	38	0.02	2.50	0.36	2.94	0.00422
49	16:26:44.3	-24:34:40.6	11.6	8.5	-24	0.01	4.10	0.23	0.33	0.00020
50	16:26:45.4	-24:19:12.9	16.4	9.8	6	0.01	3.78	0.18	0.33	0.00036

51	16:26:46.1	-24:29:13.9	32.2	14.3	54	0.02	2.91	0.23	1.07	0.00235
52	16:26:48.3	-24:20:13.6	39.7	10.2	130	0.02	2.89	0.29	1.39	0.00067
53	16:26:49.1	-24:32:02.0	9.0	8.7	84	0.01	2.95	0.17	0.16	0.00017
54	16:26:50.4	-24:23:27.3	20.5	12.4	-20	0.01	2.76	0.25	0.86	0.00136
55	16:26:51.9	-24:35:16.5	7.5	6.8	100	0.01	3.84	0.14	0.35	0.00003
56	16:26:52.6	-24:20:02.8	25.9	10.6	56	0.01	3.11	0.28	1.09	0.00103
57	16:26:52.6	-24:33:28.0	12.1	9.8	68	0.01	4.44	0.20	0.32	0.00021
58	16:26:56.6	-24:34:40.6	16.1	11.1	6	0.01	3.08	0.49	2.58	0.00047
59	16:26:58.2	-24:37:46.6	33.8	23.0	53	0.03	4.06	0.33	2.80	0.00168
60	16:26:59.6	-24:22:27.0	26.6	12.8	-18	0.02	2.72	0.18	0.55	0.00088
61	16:26:59.7	-24:29:16.9	13.8	9.5	56	0.01	2.80	0.15	0.20	0.00034
62	16:26:59.7	-24:35:12.9	10.0	7.5	45	0.00	3.51	0.19	0.15	0.00010
63	16:27:00.7	-24:22:40.4	38.1	20.8	-21	0.03	3.26	0.16	0.70	0.00084
64	16:27:02.7	-24:38:39.8	34.9	17.8	37	0.02	4.45	0.16	0.63	0.00160
65	16:27:05.5	-24:29:35.1	12.9	9.5	116	0.01	2.62	0.18	0.26	0.00023
66	16:27:06.2	-24:38:17.6	21.3	16.3	57	0.02	3.61	0.17	0.48	0.00032
67	16:27:07.2	-24:32:49.1	13.6	12.7	96	0.01	2.59	0.24	0.62	0.00039
68	16:27:07.4	-24:37:02.2	54.7	12.2	59	0.02	5.18	0.33	2.51	0.00186
69	16:27:07.8	-24:28:20.7	56.2	12.7	73	0.02	3.82	0.52	6.45	0.00250
70	16:27:08.0	-24:39:39.4	29.9	26.3	18	0.03	4.09	0.20	1.06	0.00211
71	16:27:09.9	-24:27:19.3	9.5	8.0	43	0.00	2.64	0.18	0.15	0.00011
72	16:27:10.2	-24:39:22.8	37.2	10.1	26	0.02	3.22	0.31	1.55	0.00081
73	16:27:10.5	-24:30:28.2	53.4	19.0	81	0.03	3.12	0.40	4.81	0.00205
74	16:27:10.7	-24:26:59.0	81.4	11.9	128	0.03	4.19	0.15	0.61	0.00215
75	16:27:10.9	-24:30:19.6	16.4	17.0	81	0.01	3.74	0.15	0.34	0.00063
76	16:27:11.4	-24:32:07.9	22.3	19.6	-17	0.02	3.42	0.24	1.07	0.00099
77	16:27:11.5	-24:38:07.9	33.5	19.0	38	0.02	4.62	0.26	1.61	0.00206
78	16:27:12.5	-24:25:20.7	50.0	20.0	121	0.03	3.37	0.24	1.69	0.00180
79	16:27:17.4	-24:40:58.2	19.7	15.0	0	0.01	3.16	0.20	0.60	0.00130
80	16:27:17.6	-24:42:03.6	51.7	20.0	53	0.03	3.92	0.35	3.65	0.00197
81	16:27:19.1	-24:31:42.2	25.7	12.4	95	0.01	4.20	0.19	0.54	0.00052
82	16:27:19.4	-24:29:09.6	49.5	22.8	103	0.03	4.40	0.40	5.12	0.00373
83	16:27:20.3	-24:39:51.3	19.9	12.1	39	0.01	4.55	0.30	1.23	0.00112
84	16:27:21.5	-24:26:32.0	24.5	15.2	-18	0.02	4.35	0.40	2.82	0.00117
85	16:27:22.2	-24:39:46.5	29.7	25.5	70	0.02	3.73	0.42	4.52	0.00182
86	16:27:23.8	-24:26:52.2	16.0	10.0	22	0.01	3.05	0.19	0.38	0.00025
87	16:27:24.1	-24:23:59.1	47.4	18.4	30	0.03	2.98	0.34	3.22	0.00215
88	16:27:26.4	-24:33:17.5	8.9	8.2	38	0.00	3.60	0.16	0.12	0.00012
89	16:27:27.6	-24:39:24.2	15.3	15.8	63	0.01	3.23	0.44	2.61	0.00091
90	16:27:28.0	-24:40:49.3	56.4	23.5	58	0.03	4.15	0.19	1.23	0.00151
91	16:27:29.9	-24:28:06.4	21.8	8.8	117	0.01	2.79	0.27	0.77	0.00028
92	16:27:30.4	-24:27:39.3	13.2	10.2	134	0.01	4.65	0.29	0.73	0.00044
93	16:27:30.9	-24:29:35.1	14.8	7.3	52	0.00	3.76	0.17	0.15	0.00011
94	16:27:37.0	-24:41:58.0	22.1	17.4	-16	0.02	3.97	0.16	0.48	0.00055
95	16:27:37.5	-24:27:00.1	37.3	16.1	44	0.02	3.27	0.19	0.84	0.00109
96	16:27:38.9	-24:27:07.0	34.1	15.3	62	0.02	3.84	0.30	1.89	0.00140
97	16:27:38.9	-24:35:25.9	14.8	8.7	46	0.01	2.76	0.22	0.40	0.00024
98	16:27:40.1	-24:24:37.4	26.3	19.4	104	0.02	3.20	0.41	3.53	0.00042
99	16:27:40.6	-24:41:57.6	31.1	22.6	75	0.02	3.61	0.26	1.74	0.00213
100	16:27:41.1	-24:31:60.0	7.3	8.6	78	0.00	4.27	0.19	0.10	0.00011
101	16:27:42.4	-24:24:34.7	28.1	12.7	34	0.02	3.73	0.31	1.57	0.00054
102	16:27:44.0	-24:37:18.6	20.5	11.9	118	0.01	3.18	0.28	1.03	0.00036
103	16:27:52.4	-24:31:40.0	16.2	9.8	49	0.01	4.07	0.19	0.34	0.00036
104	16:27:53.8	-24:34:53.2	14.1	11.6	112	0.01	4.16	0.18	0.34	0.00034
105	16:28:05.3	-24:36:09.4	25.0	16.0	-12	0.02	3.64	0.27	1.33	0.00076